Scattering of Coastal-Trapped Waves by Irregularities in Coastline and Topography*

JOHN L. WILKIN**

Joint Program in Oceanographic Engineering, MIT/WHOI, Woods Hole, Massachusetts

DAVID C. CHAPMAN

Woods Hole Oceanographic Institution, Woods Hole, Massachusetts

(Manuscript received 24 April 1989, in final form 27 September 1989)

ABSTRACT

The scattering of freely-propagating coastal-trapped waves (CTWs) by large variations in coastline and topography is studied using a numerical model which accomodates arbitrary density stratification, bathymetry and coastline. Particular attention is paid to the role of stratification which in moderate amounts can eliminate backscattered free-waves which occur, theoretically, in a barotropic ocean.

Numerical simulations using widening and narrowing shelf topographies show that the strength of the forward-scattering into transmitted CTW modes is proportional to a topographic warp factor which estimates the severity of the topographic irregularities. The forward-scattering is further amplified by density stratification. Within the scattering region itself, the strengths of the scattered-wave-induced currents exhibit substantial variation over short spatial scales. There is generally a marked intensification of the flow within the scattering region, and rapid variations in phase. On narrowing shelves, the influence of the scattering can extend upstream into the region of uniform topography even when no freely-propagating backscattered waves exist.

A simulation is conducted of CTW scattering at a site on the East Coast of Australia where observations suggest the presence of scattered freely-propagating CTWs. The success of the model simulation in reproducing features of observations supports the notion that realistic shelf geometries can scatter significant levels of CTW energy, and that the scattered waves can have an appreciable signal in current-meter observations made on the continental shelf. This suggests that, along irregular coastlines, it is important to account for the possibility that CTW scattering may be occurring if oceanographic observations are to be interpreted correctly.

1. Introduction

Over the past twenty years, oceanographic observations have revealed that patterns of sea-level and current fluctuations with periods of a day or more propagate along the continental shelves of many of the world's oceans. These subinertial-frequency wavelike motions, which extend across the width of the shelf and are often generated by winds many hundreds of kilometers from where they are observed, account for a major part of the large-scale, low-frequency current and sea-level variability along many coastlines. Theoretical studies have attributed these motions to wind-driven and/or freely propagating coastal-trapped waves (CTWs) which travel cyclonically with respect to the deep sea, i.e. with the coast on the right (left) in the Northern (Southern) Hemisphere.

Statistical analyses of sea-level, current and wind data combined with models of CTW dynamics along the coast of Peru (Smith 1978), the west coast of North America (Halliwell and Allen 1987) and the East Australian coast (Freeland et al. 1986; Church et al. 1986a) confirm that the waves observed there have speeds and across-shelf structures consistent with those expected from theoretical analyses. Further validation of CTW theory is provided by applications of the first-order wave equation (FOWE) method (e.g. Clarke and Van Gorder 1986) in situations where the long wave approximation can be made (i.e., wave periods are in the range of several days to a few weeks and alongshelf scales of motion are much greater than the shelf width). Along relatively straight coasts, the FOWE studies of Battisti and Hickey (1984), Church et al. (1986b), Chapman (1987), and Mitchum and Clarke (1986) obtained generally good agreement between observed and hindcast sea-level and alongshelf current fluctuations.

However, most coastlines vary significantly over spatial scales much shorter than CTW length scales

* WHOI Contribution Number 7115.

** Present affiliation: New Zealand Oceanographic Institute, Wellington, New Zealand.

Corresponding author address: Dr. John L. Wilkin, Department of Scientific and Industrial Research, Division of Water Sciences, Private Bag, Kilbirnie, Wellington 3, New Zealand.

© 1990 American Meteorological Society

which introduces the possibility of appreciable scattering of CTW energy from one mode into others occurring over alongshelf distances comparable to the shelf width, a process not accounted for in FOWE analyses. For example, the poorest agreement between observations and the time series hindcast by Mitchum and Clarke (1986) occurs at the northern end of the West Florida shelf where the shelf narrows abruptly. Chapman (1987) found that the propagation of CTWs through the irregular geometry south of Point Conception, California, where the shelf widens abruptly, the coastline bends sharply and the coastal waveguide is split by a chain of offshore islands, was not modelled adequately by FOWE dynamics. Observations by Griffin and Middleton (1986) suggest the possible generation of high mode CTWs in the lee of Fraser Island, Australia.

While likely to have a significant effect on the propagation of CTWs, scattering processes at places where the shelf width and topography change sharply are poorly understood. To date, most studies of CTW scattering have been limited to the scattering of Kelvin waves by small or abrupt coastline variations in a uniformly stratified ocean without coastal topography (e.g. Mysak and Tang 1974; Buchwald 1968; Packham and Williams 1968), and to the scattering of barotropic shelf waves (the weak stratification limit of CTWs) by slowly varying, small or randomly placed small changes in topography and coastline (e.g., Killworth 1978; Buchwald 1977; Allen 1976; Chao et al. 1979; Brink 1980). The scattering of long CTWs by small bottom irregularities in a stratified ocean was considered by Brink (1986).

A few studies have considered the scattering of barotropic shelf waves (BSWs) by large variations in coastline and topography. Of particular interest to the present study is the work of Hsueh (1980) who showed that large variations in shelf width occurring over large alongshelf distances (i.e., where the longwave approximation is valid) will not scatter BSWs if the topography varies in a "shelf-similar" manner where the distance from each isobath to the coast remains a fixed fraction of the local shelf width. Hsueh (1980) proceeded to consider scattering due to small deviations from shelf-similarity, and found that scattering could create across-shelf phase differences in flow events comparable to the phase differences found by Brink and Allen (1978) which were due to bottom friction effects. Davis (1983) showed that the restrictive longwave approximation need not be made in the definition of shelf-similar topographies. Using conformal mapping arguments he demonstrated that any shelf topography can be mapped to one of constant width in the new mapped coordinate, and that the equation governing the propagation of dispersive BSWs is invariant under such a mapping. Furthermore, Davis showed that if the logarithm of the depth satisfies Laplace's equation, then the shelf maps to a shelf of constant width with parallel isobaths which, therefore, will not scatter BSWs. This property is the foundation of Hsueh's definition of shelf-similarity. Strictly speaking, Hsueh's definition is not valid for shelf width changes which occur over an alongshelf distance comparable to the shelf width, and Davis' more rigorous definition should be applied. However, inspection of Davis' example (Davis 1983, his Fig. 1) in which the shelf width changes by a factor of 1.5 over a distance twice the mean shelf width, it is clear that the definitions are almost identical. In the long wave limit the two definitions coincide. It should be stressed that this property holds only in the barotropic limit. With the introduction of stratification, the governing equation is no longer invariant under conformal transformations and the possibility of CTW scattering cannot be ruled out.

Other studies of BSW scattering by large variations in coastline and topography include the work of Webster (1987) who considered topography which is shelf-similar in the sense defined by Hsueh (1980) but varying over an alongshelf distance comparable to the shelf width. As expected from Davis' (1983) analysis, the scattering of BSWs was weak unless the relative change in shelf width was large and the length of transition zone was less than the shelf width. Wang (1980) considered the scattering of a BSW by a canyon, a ridge, or diverging/converging isobaths. Little backscattering occurred for the cases of convergence or divergence of depth contours unless the incident wave frequency exceeded the maximum possible frequency of all outgoing modes, in which case total reflection resulted. The canyon and ridge topographies both backscattered a large portion of the incoming wave energy. Wilkin and Chapman (1987) presented a solution for the scattering of a BSW incident upon a discontinuity in shelf width. They found a substantial transfer of energy to modes other than that of the incident wave which produced a strong modulation in flow intensity and phase progression downstream of the scattering region. Middleton and Wright (1988) considered BSW scattering by an abrupt jump in depth. Energy transmission was greatest at low frequencies and decreased with increasing frequency and increasing jump size. A review of other studies is presented by Huthnance et al. (1986).

While the above BSW results are useful for developing insight into scattering processes, the neglect of stratification may be a serious omission. Huthnance (1978) and Chapman (1983) have shown that the introduction of weak stratification can eliminate the backscattered free waves found in a barotropic ocean. In such a case, there can be no backscattering and the BSW results may be qualitatively altered. We address this issue by using the numerical model described in section 2 to consider the problem of CTW scattering by large variations in coastline and topography occurring over alongshelf distances comparable to the shelf width in a realistically stratified coastal ocean (section 3). Then, in section 4, the numerical model is used to

simulate CTW scattering at a site on the East Coast of Australia where observations made by Griffin and Middleton (1986) suggest the presence of scattered freely-propagating CTWs.

2. The numerical model

The numerical experiments discussed in section 3 were conducted using the four-dimensional (x, y, z, t), primitive equation, ocean circulation model developed by D. Haidvogel of Johns Hopkins University. The Haidvogel primitive equation model (PEM) is ideally suited for studies of CTW scattering because it allows for the specification of: (i) irregular coastal geometry through the use of boundary-fitted orthogonal curvilinear coordinates in the horizontal, (ii) irregular bottom topography by employing a stretched "sigma" coordinate in the vertical, (iii) arbitrary density stratification, and (iv) arbitrary open boundary conditions. The formulation, implementation and testing of the PEM have been documented in detail by Haidvogel et al. (1990). A brief outline of the modifications made to tailor the PEM to the present application is presented here. A more complete description may be found in Wilkin (1988a).

a. Simplifications to the governing equations

The primitive equations are derived from the incompressible Navier–Stokes equations of fluid flow by making the Boussinesq and hydrostatic approximations (e.g. Cox 1985). In order to study freely propagating linear inviscid CTWs the nonlinear terms and vertical diffusion terms of the primitive equations were omitted from the numerical calculations. Strictly speaking, the horizontal mixing terms should also be omitted, but as is frequently found in primitive equation models, some horizontal friction must be retained in the momentum equations to control small-scale computational noise.

b. Orthogonal curvilinear coordinates

The physical domain of the numerical experiments is typically, although not necessarily, bounded by an irregular coastline, a straight offshore boundary, and two straight across-shelf open boundaries. The computer code used in the present application to generate the curvilinear grids fitted to the domain (Wilkin 1988b) is based on an algorithm described by Ives and Zacharias (1987) which first maps the irregular geometry to a rectangle using repeated applications of a power (or hinge point) conformal transformation. Once the boundary mapping is complete, the grid can be filled in by solving Laplace's equation for the physical coordinates of the grid points. The metric factors of the coordinate transformation can then be calculated and input into the model. An example of one of the coordinate grids used in the experiments is shown in Fig. 10.

c. Coastal-trapped wave across-shelf modal structures

In order to introduce free CTWs into the PEM, and to identify scattered CTWs in the model output, it is necessary first to compute their across-shelf modal structures. This is achieved by using an algorithm (Wilkin 1987) developed specifically for use in conjunction with the PEM which computes the modal structures of free CTWs for arbitrary bottom topography and stratification using the same numerical discretization scheme employed in the PEM.

Making the approximations outlined above (i.e., linear, inviscid, hydrostatic, Boussinesq), the equation governing the across-shelf modal structure of the pressure perturbation of a free CTW [$\hat{\phi}(\eta, z)$] with wavenumber k and frequency ω is

$$n \frac{\partial}{\partial \eta}\left(n \frac{\partial \hat{\phi}}{\partial \eta}\right) + (f^2 - \omega^2) \frac{\partial}{\partial z}\left(\frac{1}{N^2} \frac{\partial \hat{\phi}}{\partial z}\right) - k^2 \hat{\phi} = 0 \quad (1)$$

where η is the across-shelf coordinate, n is the metric coefficient function (in the η direction) of the curvilinear coordinate transformation, f is the Coriolis frequency, and $N^2(z)$ is the square of the Brunt–Väisälä frequency, assumed to vary only with vertical coordinate z. It is assumed that the bottom depth profile h varies only in the across-shelf direction at the location at which the modal structures are to be computed.

For a given h, N^2, f and k there is a sequence of solutions to (1), subject to appropriate boundary conditions, at discrete eigenfrequencies $\omega_1, \omega_2, \omega_3 \ldots$ which are free CTWs (e.g., Huthnance 1978).

d. The numerical wavetank

The numerical experiments were conducted by combining the model components described above into what may be described as a "numerical wavetank" (Fig. 1). The wavetank is enclosed by four boundaries. Along the coastal wall a boundary condition of no normal flow is applied. For computational convenience, the offshore boundary is also treated as a free-slip wall. The wall is placed well offshore—typically 2 to 3 times the shelf width—and moving it farther offshore produces negligible change in the CTW dispersion curves. The incident wave is introduced into the computational domain by a numerical "wavemaker" which prescribes the horizontal velocity components and density perturbation at each time step at the upstream across-shelf boundary. The prescription is a simple harmonic time-modulation of the incident-wave modal structure. The simulations begin with a quiescent wavetank and, to minimize initial transients, the wavemaker amplitude increases smoothly over one wave period to a constant value. As the wave propagates through the width change, it scatters into a set of transmitted waves of

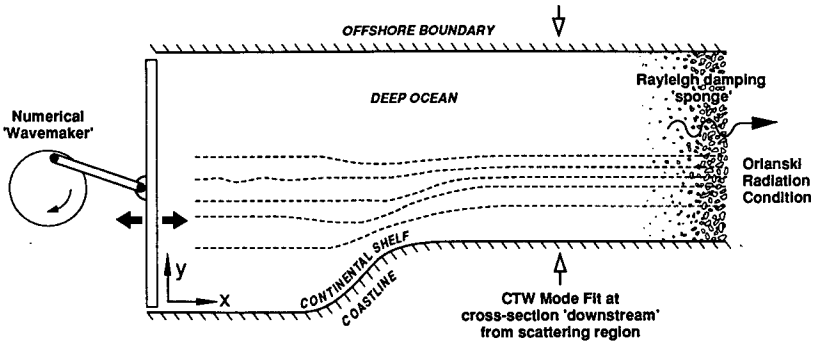

FIG. 1. The "numerical wavetank" configuration of the numerical model. The tank is bounded by free-slip lateral walls. A free coastal-trapped wave is introduced by a wavemaker at the upstream (left) end of the tank. Scattered waves propagate out through the radiation boundary at the downstream end of the tank.

different modes. An Orlanski (1976) radiation condition combined with a Rayleigh damping sponge at the downstream across-shelf boundary allows the scattered waves to propagate out of the computational domain with little reflection.

The horizontal spatial resolution of the model is set when the curvilinear coordinate grid is generated. The model runs reported in section 3 were conducted with an alongshelf grid spacing of approximately 15 km, an across-shelf spacing of 4 to 6 km, and seven Chebyshev polynomials in the vertical. Tests of CTW propagation in a straight channel with periodic open boundary conditions showed that for spatial resolution of this order, root-mean-square errors in the horizontal velocity components after one wave period were at most a few percent for the low modes (Haidvogel et al. 1990).

Laplacian diffusion applied on constant sigma surfaces was employed to damp out the small-scale (two grid point) computational noise which arises in the simulations. The Laplacian operator includes both alongshelf (ξ) and across-shelf (η) terms. It was found that, by using a large diffusion coefficient ($500\ \mathrm{m^2\,s^{-1}}$) for the alongshelf term and a smaller value ($100\ \mathrm{m^2\,s^{-1}}$) for the across-shelf term, the noise could be controlled without significantly affecting the propagation of the CTWs. No damping was applied to the density equation.

e. *Analysis: Modal decomposition*

In order to understand the simulated CTW scattering, the amplitudes of the scattered modes were extracted from the PEM output. This was achieved by performing a least squares fit of the model output to a sum of propagating CTW modes downstream from the scattering region. Evanescent motions trapped at the scattering region have an alongshelf decay scale comparable to the across-shelf scale of the topography or the largest deep-ocean internal Rossby radius (corresponding to the lowest internal mode), whichever is greater. In practice, the topographic length scale almost always dominates, so provided the modal fit is performed 200 to 300 km downstream of the scattering region, the motions present are due virtually solely to freely propagating scattered CTWs.

The mode fit is performed using the alongshelf velocity which has a strong signal for all stratifications and topographies. Let ξ_0 be the alongshelf location at which the fit is performed. At ξ_0 the grid must be rectangular and the topography must vary only with η. The alongshelf velocity field calculated by the PEM is represented as

$$u_{\mathrm{PEM}}(\xi_0, \eta, z, t) = \sum_{q=1}^{Q} B_q(\xi_0, t) U_q(\eta, z) + \epsilon(\xi_0, \eta, z, t) \quad (2)$$

where $U_q(\eta, z)$ is the modal structure of the alongshelf velocity of transmitted mode q and $B_q(\xi_0, t)$ is the instantaneous amplitude of mode q at time t. The residual error between the CTW mode fit and the PEM output is $\epsilon(\xi_0, \eta, z, t)$. A total of Q transmitted modes is included in the analysis. Once the initial transients have passed (typically three wave periods), and provided the section ξ_0 is not too close to the Rayleigh sponge, the modal decomposition returns time series of $B_q(\xi_0, t)$ values which are periodic with the frequency of the incident wave.

Integrating ϵ^2 over the vertical across-shelf plane at ξ_0 gives the square of the total residual error in the mode fit. Minimizing the total residual error results in a set of simultaneous equations for the time series of the mode amplitudes which may be written

$$\sum_{q=1}^{Q} A_{mq} B_q(\xi_0, t) = r_m \quad m = 1, 2 \cdots Q \quad (3)$$

where

$$A_{mq} = \int_0^{\eta_{\max}} \int_{-h}^{0} U_m(\eta, z) U_q(\eta, z) dz d\eta \quad (4)$$

$$r_m = \int_0^{\eta_{\max}} \int_{-h}^{0} U_m(\eta, z) u_{\mathrm{PEM}}(\xi_0, \eta, z, t) dz d\eta. \quad (5)$$

In practice, the integrations over η and z in (4) and (5) are performed numerically. The magnitude of each harmonic series $B_q(\xi_0, t)$ gives the amplitude of the corresponding CTW mode. The normalization of the $U_q(\eta, z)$ modal structures is performed so that the energy flux of each mode, integrated across the shelf, is given by the amplitude squared.

f. Model performance test: Comparison with analytical results

A simulation of BSW scattering which nearly duplicates the problem considered by Wilkin and Chapman (1987) was conducted by Wilkin (1988a) as a test of the numerical wavetank configuration of the PEM and the modal decomposition method. (The details of the test are also reported by Haidvogel et al. 1990.) The least-squares fit gave amplitudes for modes 1 through 4 as 0.365, 0.457, 0.286 and 0.073, which compare favorably with the analytical values of 0.346, 0.461, 0.316 and 0.085, respectively (Wilkin and Chapman 1987, their Table 1). The discrepancy is consistent with the necessarily smoother coastline change used in the PEM being slightly less conducive to scattering into higher modes. From this test it was concluded that the PEM can be applied reliably to the simulation of BSW scattering by irregular coastal geometry, and that the modal fit method accurately extracts the mode amplitudes from the model output. Other tests of the PEM (Haidvogel et al. 1990) show that the model correctly propagates CTWs in a stratified coastal ocean. Furthermore, as will be seen in the following sections, energy flux is nearly conserved in all of the scattering calculations. There is every indication, therefore, that the model can be used with confidence in the simulation of CTW scattering processes.

3. Numerical results and discussion

a. CTW dispersion properties and scattering regimes

The dispersion properties of free CTWs play a key role in their behavior as they propagate through an irregular waveguide. Indeed, it is possible to deduce several net energy transmission properties of a particular scattering geometry by simply examining the dispersion curves of free CTWs at each end of the scattering region without detailed consideration of the dispersion properties within the scattering region itself.

Consider the two across-shelf depth profiles shown in Fig. 4a. The dispersion curves of the mode 1 CTWs for these two topographies, for different stratifications (i.e., different constant values of N^2), are shown in Fig. 2. The curves, computed using the algorithm of Wilkin (1987), illustrate the theoretical result derived by Huthnance (1978) that increasing the stratification increases the wave frequency at all wavenumbers. Huthnance (1978) also showed that, as the wavenumber (k) becomes large, the frequency (ω) tends to a constant value provided the bottom slope remains bounded. This limiting frequency is given by

$$\omega_\infty = \lim_{k\to\infty} \omega = \max_y \left[N|_{z=-h(y)} \frac{dh}{dy} \right] \quad (6)$$

where y is the across-shelf coordinate. The frequency of every mode converges to this limit.

For weak stratifications, $\omega(k)$ has at least one stationary point ω_c where ω takes a local maximum. There is therefore a range of frequencies for which CTWs

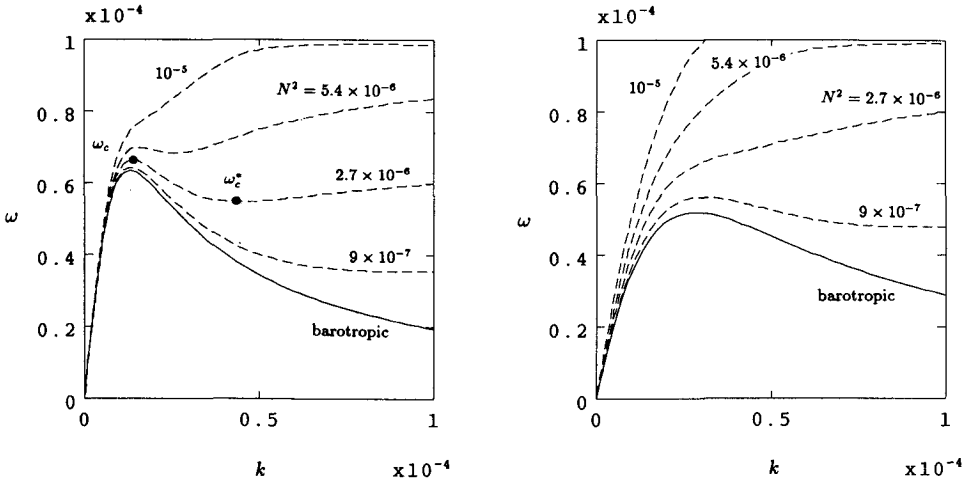

FIG. 2. Mode 1 CTW dispersion curves for the (left) wide and (right) narrow topographies shown in Figure 4a computed for different constant values of N^2, for $f = 10^{-4}\ \mathrm{s}^{-1}$. Curves are labeled with N^2 values in units s^{-2}. The stationary points of $\omega(k)$ defined in the text, i.e., ω_c and ω_c^*, are illustrated on the $N^2 = 2.7 \times 10^{-6}\ \mathrm{s}^{-2}$ curve in the left panel.

with negative group velocity can exist. Within this class, there is a range of stratifications for which $\omega(k)$ may also take a local minimum, ω_c^*, for one or more of the lowest modes. The value of ω_c^* for the highest mode with a local minimum frequency is the lowest frequency at which a CTW with negative group velocity can occur. If there are no local minima, then the lower bound for negative group velocity waves is simply ω_∞. The maximum frequency at which a wave with positive group velocity exists is given by the maximum of ω_c and ω_∞.

As the strength of the stratification increases, a qualitative change in the form of the curves occurs, from dispersion curves which have a region of negative slope, to dispersion curves without any negatively sloping region. This second class of dispersion curves occurs at moderate to high stratification. In this case the curves increase monotonically to the limiting value ω_∞ so that there are no free waves above ω_∞ and no waves at all with negative group velocity.

The significance of these limiting frequencies to CTW scattering becomes apparent when the limits for two different topographies are compared as functions of stratification. The dashed lines in Fig. 3 show the limiting frequencies for the wide and narrow topographies, shown in Fig. 4a. The ω_c values were taken directly from Fig. 2 and ω_∞ was calculated from (6). The minimum ω_c^* values are shown only schematically since their evaluation would require the computation of dispersion curves for many modes at many stratifications. If, in the direction of CTW propagation, the shelf bathymetry makes a smooth transition from the wide to the narrow topography then the various frequency limits imply the existence of the scattering regimes shaded in Fig. 3a. Consider a slice through Fig. 3a at some constant low value of N: At very high frequencies there are no waves with positive group velocity on the wider shelf. In this case an incident wave cannot exist and the question of how it might scatter is moot. Below the wide shelf cutoff frequency ($\omega_{c,\ \mathrm{wide}}$) but above the narrow shelf cutoff frequency ($\omega_{c,\ \mathrm{narrow}}$), there is a range where an incident wave is possible but there are no waves with positive group velocity on the narrow shelf. Therefore, in this range there are no waves able to transport energy into the region of narrow topography and the energy flux of the incident wave must be totally reflected. At lower frequencies there is a range where both incident and transmitted waves exist and partial reflection of CTW energy is possible though by no means assured. At still lower frequencies [i.e., $\omega < \min(\omega_{c,\ \mathrm{wide}}^*, \omega_{\infty,\mathrm{wide}})$] there are no waves with negative group velocity on the wider shelf, so reflection is impossible and all the incident wave energy flux must be scattered forward into the CTW modes of the narrow shelf. If the topographic transition is in the opposite sense, i.e., narrow to wide, each limiting frequency line assumes a different significance and the resulting scattering regimes are as shown in Fig. 3b. In this case transmitted waves exist for all frequencies at which an incident wave is possible and the region of total reflection is absent.

The statistical analyses cited in section 1 show that the energy of observed CTW motions is generally located in a band of frequencies corresponding to periods of a few days to a few weeks. In coastal oceans, average values of N^2 are typically in the neighborhood of 10^{-6} to 10^{-5} s^{-2}. For this range of parameters, i.e., $\omega < 2 \times 10^{-5}$ s^{-1}, $10^{-3} < N < 3 \times 10^{-3}$ s^{-1}, inspection of Fig. 3 suggests that regardless of whether the shelf widens or narrows, CTWs should not be reflected by the

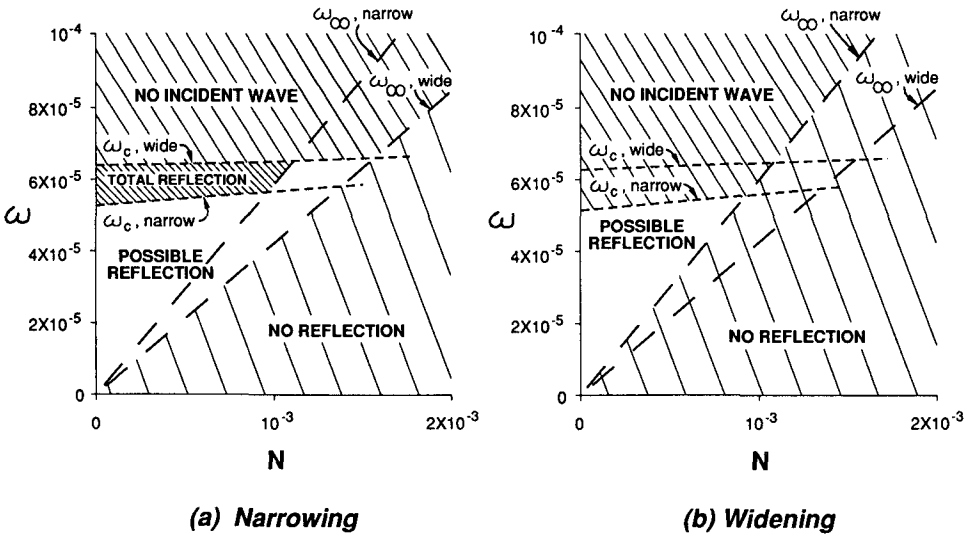

FIG. 3. Scattering regimes for shelf bathymetries which, in the direction of CTW propagation, make a transition from the (a) wide to the narrow, and (b) narrow to the wide topographies shown in Fig. 4a.

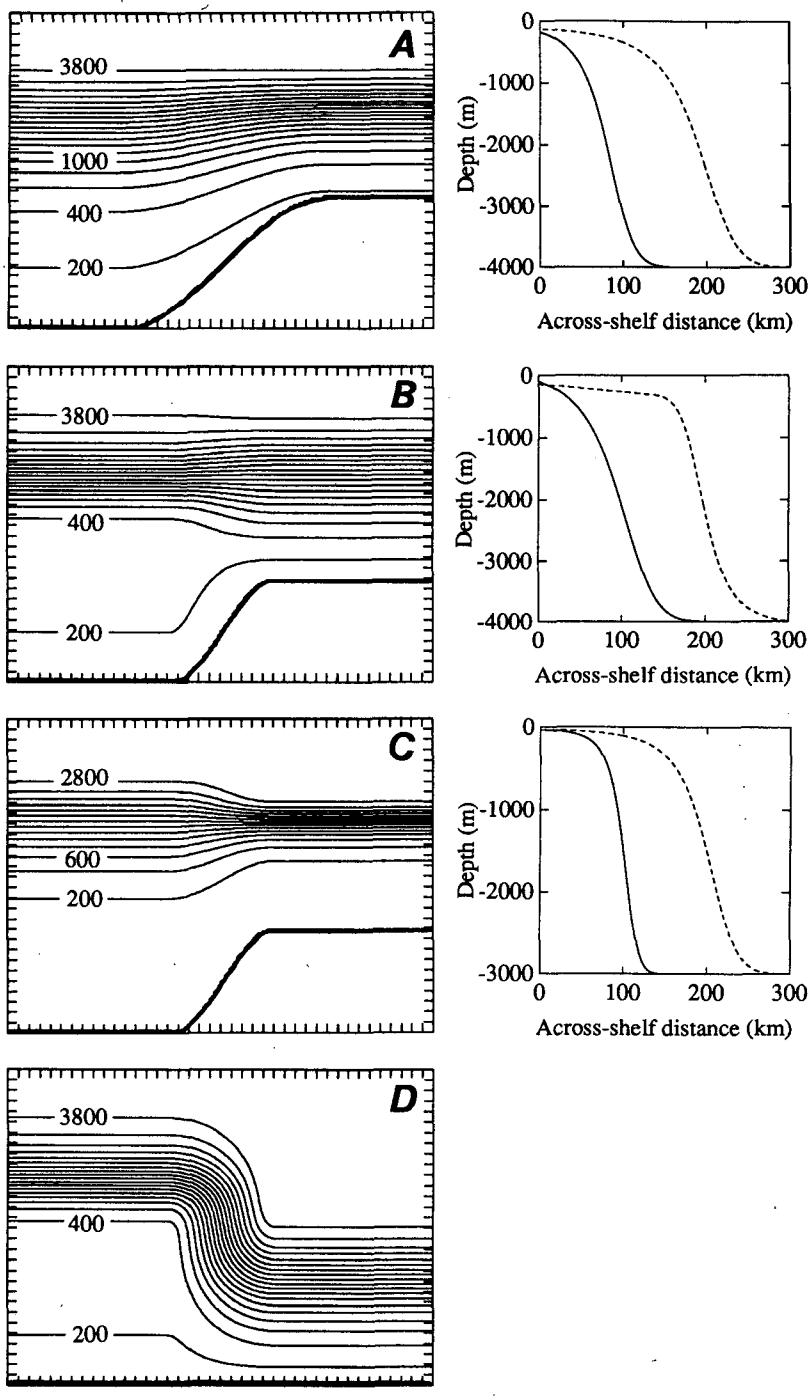

FIG. 4. Bathymetries used in the narrowing shelf scattering experiments. Depth contour interval is 200 m in each figure. Tick marks are at 10 km spacing. Heavy solid line is the coast. The depth profiles outside the scattering region are shown at right for each case (dotted line is the depth profile at the left (incident) end of the channel, solid line is the depth profile at the right end of the channel). (a) Bathymetry used in the first series of narrowing shelf scattering experiments. (b) Bathymetry used in the second series of experiments. (c) Shelf-similar bathymetry used in the third series of experiments. (d) Bathymetry used in the fourth series of experiments. [The depth profiles outside the scattering region for case (d) are the same as those in (a).]

topographic variation. This illustrates the basis for the assertion made in section 1 that the results of BSW scattering studies which show significant reflection of BSW energy may be qualitatively altered by the introduction of stratification. It should be emphasized at this point that Fig. 3 is based on the topographies shown in Fig. 4a and uniform stratifications (N independent of depth). For other topographies and stratification profiles, the boundaries of the scattering regimes are similar qualitatively but differ quantitatively due to differences in the details of the dispersion curves.

While this analysis is useful for identifying gross properties of the CTW scattering process such as total energy transmission or reflection, it provides no information about what proportion of the incident energy is scattered into each of the transmitted CTW modes, or how much reflection can be expected in the regions labelled "possible reflection". Furthermore, there is no consideration of the details of the flow field within the scattering region. To address these issues it is necessary to proceed to the numerical experiments.

b. *Narrowing shelf results*

1) A NARROWING TOPOGRAPHY

The first series of numerical simulations examines the scattering of CTWs by the bathymetry plotted in Fig. 4a. The shelf narrows by 125 km over an alongshelf distance of 200 km with most of the variation occurring at the coast while the continental slope remains relatively straight. The average shelf width (i.e., the mean of the distances from the coast to the region of uniform depth measured at the ends of the scattering region) is 225 km and the channel is 425 km wide at its widest (incident) end. The case of a mode 1 incident wave with frequency 1×10^{-5} s^{-1} (f is fixed at 10^{-4} s^{-1} throughout, so $\omega = 0.1f$ in this case) and uniform stratification $N^2 = 2.7 \times 10^{-6}$ s^{-2}, is in the "no reflection" regime of Fig. 3a, so the energy flux in the transmitted waves should balance the incident energy flux. As is typical of all the numerical simulations reported here, the length of the scattering region is only a small fraction of the wavelength of the incident wave. For the present case, the incident wave has a wavenumber of 9.5×10^{-7} m^{-1} corresponding to a wavelength of over 6500 km. The magnitudes of the least squares mode-fit time series for this case, computed as described in section 2, are 0.973, 0.309 and 0.125 for modes 1 through 3 respectively, which give energy fluxes of 0.948, 0.096 and 0.016 and a total transmitted energy flux of 1.065. The energy in the higher modes is negligible. Since the incident wave has unit energy flux it is apparent that the model overestimates the energy of the scattered waves by some 6%. A 6% error in energy corresponds to roughly 3% errors in the mode amplitudes. This error level is comparable to that determined by Haidvogel et al. (1990) in their tests of CTW propagation in a straight periodic channel version of the PEM.

The effect that stratification has on the strength of the scattering was examined by repeating the above simulation for several values of N^2 (Table 1). In all cases the modal-fit overestimated the total transmitted energy by 5% to 7%, so the individual transmitted mode energy fluxes have been normalized by the modal fit total energy flux. For completeness, the total energy flux values returned by the modal fit are shown in the bottom row of Table 1. The differences between these values and unity indicate the accuracy of the other entries in the table.

The results show clearly that increasing stratification amplifies the scattering process—the energy flux remaining in mode 1 diminishes with increasing stratification while that in mode 2 increases. Overall however, the strength of the scattering is not pronounced, especially in the barotropic ($N^2 = 0$) case where the incident mode loses only 7% of its energy flux. This may seem surprising at first, given the large change in shelf width. It is less surprising when the idea of "shelf-similarity" (section 1) is recalled. A shelf-similar topography will not scatter long BSWs, and the bathymetry used in this series of experiments (Fig. 4a) departs only moderately from the definition of shelf-similarity given by Hsueh (1980).

2) LESS SHELF-SIMILAR TOPOGRAPHY

For the second series of simulations, the depth profiles outside the scattering region are markedly different (Fig. 4b), in contrast to the previous series of experiments. The wider shelf has a broad region which slopes gently away from the coast but drops off abruptly to abyssal depths, whereas the narrower shelf is more uniformly sloping with a less pronounced shelf break. Consequently, as the shelf narrows over an alongshelf distance of 100 km (i.e., more abruptly than in the first series of experiments) some isobaths are displaced shoreward while others move offshore. This bathymetry therefore departs strongly from Hsueh's (1980) definition of shelf-similarity. In a series of experiments

TABLE 1. Energy fluxes of the transmitted modes generated when a mode 1 incident wave with frequency 1×10^{-5} s^{-1} encounters the variable topography of Fig. 4a for different values of uniform stratification (N^2). More energy is lost from mode 1 (i.e., scattering increases) as the stratification increases. The total transmitted energy flux computed by each modal fit and used to normalize the other table entries (see text) is shown in parentheses in the final row.

	N^2 (s^{-2})			
Mode	0	9×10^{-7}	2.7×10^{-6}	5.4×10^{-6}
1	0.932	0.915	0.890	0.877
2	0.060	0.074	0.090	0.094
3	4.4×10^{-3}	0.019	0.015	0.017
4	—	7.6×10^{-4}	5.1×10^{-3}	9.3×10^{-4}
	(1.050)	(1.069)	(1.065)	(1.067)

analogous to the first series, the scattering of a mode 1 incident wave with frequency 1×10^{-5} s^{-1} was examined for a range of stratifications (Table 2). As in the previous experiments, stratification amplifies the strength of the scattering. Comparison with Table 1 shows that at all stratifications the scattering is more pronounced for this less-shelf-similar topography—more than 20% of the incident mode energy flux is transferred to higher modes when the stratification reaches the still modest level of $N^2 = 5.4 \times 10^{-6}$ s^{-2}.

3) SHELF-SIMILAR TOPOGRAPHY

As noted in section 1, BSWs should propagate through shelf-similar topographic variations without scattering. However, with the introduction of stratification this property may no longer hold, and scattering may occur. Therefore, the third series of scattering experiments considers the scattering of a CTW by a topography (Fig. 4c) which is exactly shelf-similar in the sense described by Hsueh (1980).

As in the previous two series of experiments, the incident wave is mode 1 and has a frequency of 1×10^{-5} s^{-1}. At all the stratifications considered there is practically no scattering of energy into modes other than that of the incident wave (Table 3), even for stratifications stronger than those considered previously. Therefore, the introduction of stratification does not, of itself, appear to cause CTWs to scatter on a shelf where scattering is not induced in the barotropic limit. These results suggest that the role of stratification in CTW scattering processes is one of modifying the scattering triggered by nonshelf-similar topographic irregularities.

4) COASTLINE EFFECTS

The irregular topographies considered up to this point can be characterized as abrupt narrowings of the shelf due primarily to variations in the position of the coastline. In all cases the continental slope remains relatively straight. However, the vorticity gradient that contributes to the support of CTWs is greatest where the across-shelf bottom slope is steepest. Therefore, one might expect that variations in the position of the continental slope would act as more severe irregularities in the CTW waveguide than comparable displacements of the coastline. The following series of experiments confirms that this is the case.

In this set of simulations the depth profiles outside the scattering region are identical to those of the shelf shown in Fig. 4b, but the transition between the two profiles, which occurs over an alongshelf distance of 100 km, is achieved without any change in the position of the coast (Fig. 4d). The energy fluxes in the transmitted modes, for an incident mode 1 wave with frequency 1×10^{-5} s^{-1} (Table 4) confirm that the incident mode loses somewhat more energy in this case than in the corresponding straighter-continental-slope case (Table 2).

An additional run was made for the $N^2 = 2.7 \times 10^{-6}$ s^{-2} case with the alongshelf distance separating the two different shelf profiles (i.e., the length of the scattering region) increased to 200 km. This doubling of the length of the scattering region produced changes of less than 1% in the energy fluxes of scattered modes 1 and

TABLE 2. Energy fluxes of the transmitted modes generated when a mode 1 incident wave of frequency 1×10^{-5} s^{-1} encounters the variable topography of Fig. 4b for different values of the stratification (N^2). Table entries are calculated in the same manner as Table 1. Scattering is stronger (i.e., more energy is lost from the incident mode) than for the topography of Fig. 4a.

	N^2 (s^{-2})			
Mode	0	9×10^{-7}	2.7×10^{-6}	5.4×10^{-6}
1	0.877	0.847	0.803	0.795
2	0.119	0.147	0.182	0.169
3	4.7×10^{-3}	4.7×10^{-3}	0.014	0.031
4	6.3×10^{-3}	1.5×10^{-3}	2.9×10^{-4}	4.8×10^{-3}
	(1.037)	(1.046)	(1.040)	(1.032)

TABLE 3. Energy fluxes of the transmitted modes generated when a mode 1 incident wave of frequency 1×10^{-5} s^{-1} encounters the shelf-similar topography of Fig. 4c for different values of the stratification (N^2). Table entries are calculated in the same manner as Table 1. For this topography there is no appreciable scattering at any stratification.

	N^2 (s^{-2})				
Mode	0	1.8×10^{-6}	2.7×10^{-6}	5.4×10^{-6}	1×10^{-5}
1	0.993	0.994	0.993	0.988	0.982
2	2.8×10^{-3}	2.1×10^{-3}	2.9×10^{-3}	7.7×10^{-3}	0.016
3	3.4×10^{-3}	3.5×10^{-3}	3.4×10^{-3}	2.0×10^{-3}	9.6×10^{-4}
4	—	4.1×10^{-4}	7.2×10^{-4}	1.5×10^{-3}	1.6×10^{-3}
	(1.057)	(1.063)	(1.061)	(1.062)	(1.048)

TABLE 4. Energy fluxes of the transmitted modes generated when a mode 1 incident wave of frequency 1×10^{-5} s^{-1} encounters the variable topography of Fig. 4d for different values of the stratification (N^2). Table entries are calculated in the same manner as Table 1. The shelf profiles outside the scattering region are the same as for the case considered in Table 2 but the scattering is stronger here because the transition between the two profiles occurs primarily as a displacement of the shelf-slope break.

	N^2 (s^{-2})				
Mode	0	9×10^{-7}	2.7×10^{-6}	5.4×10^{-6}	1×10^{-5}
1	0.854	0.800	0.758	0.746	0.730
2	0.139	0.181	0.209	0.213	0.194
3	6.9×10^{-3}	0.017	0.025	0.037	0.052
4	1.8×10^{-8}	1.7×10^{-3}	7.4×10^{-3}	4.5×10^{-3}	0.024
	(1.013)	(1.028)	(1.020)	(1.016)	(0.967)

2. This suggests that the strength of the scattering induced by shelf width changes is not sensitive to the alongshelf length of the scattering region provided the length is much less than the CTW wavelength.

5) SCATTERING COEFFICIENT

The scattering properties of the four topographies considered in the simulations above can be compared by defining a scattering coefficient C_{sc}:

$$C_{sc} = 1 - \frac{\text{Energy flux in transmitted mode 1}}{\text{Total transmitted energy flux}} \quad (7)$$

If the incident mode 1 wave passes through the scattering region without loss of energy then $C_{sc} = 0$, and if the incident mode loses energy to other transmitted modes, C_{sc} is greater than zero.

Recalling the earlier result that the effect of stratification is one of modifying the scattering triggered by nonshelf-similar topography, an appropriate empirical form for the scattering coefficient is

$$C_{sc} = W(h)[1 + G(S)]. \quad (8)$$

Here, $W(h)$ represents the scattering induced by topographic variation alone; if the topography is shelf-similar, then $W(h) = 0$ and C_{sc} is zero regardless of the stratification. The function $G(S)$, where S is some measure of the strength of the stratification, should be zero at zero stratification and increase with S so that the factor $[1 + G(S)]$ accounts for the amplification of the scattering observed in the numerical experiments.

In CTW theory (e.g., Huthnance 1978; Chapman 1983), the strength of the stratification is measured by the Burger number $S = NH/fL$, where L is the across-shelf distance from the coast to flat-bottom deep ocean and H is the depth of the deep ocean. A simple form for G is found when C_{sc} values calculated from the numerical results for non-shelf-similar topographies, normalized by the zero stratification value for each topography, are plotted against S (Fig. 5). (This should be equivalent to plotting $C_{sc}/W(h)$ vs S.) The value of L used to compute S is the average shelf width (i.e., the mean of the distances from the coast to the region of uniform depth measured at the ends of the scattering region). The simulation results for every topography fall close to a single straight line, indicating that for the moderate values of S considered here, G is an approximately linear function, say $G = \beta S$. The straight line passing through $G(0) = 0$ which best fits the data in Fig. 5 has slope $\beta = 2.01$.

The function $W(h)$ measures the amount of scattering that occurs at zero stratification. From the works of Hsueh (1980) and Davis (1983), $W(h)$ should be related to the extent to which the topography departs from shelf-similarity, and may therefore be thought of as being proportional to some topographic "warp" factor. An approximate form for the warp factor can be

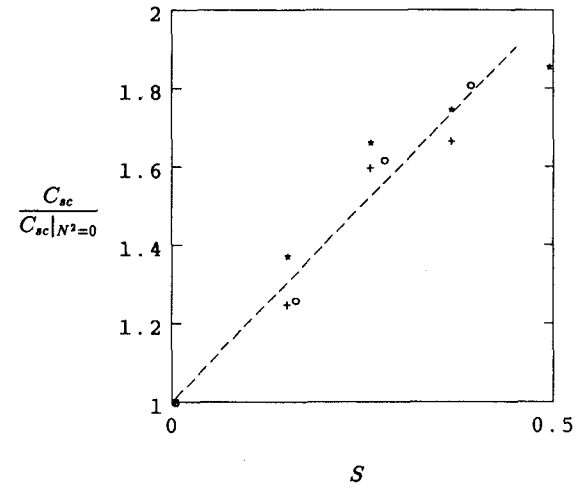

FIG. 5. Scattering coefficient C_{sc} values for the nonshelf-similar topographies, normalized by $C_{sc|N^2=0}$, vs Burger number $S = NH/fL$. This is equivalent to plotting $C_{sc}/W(h)$ [see Eq. (7)], and shows that the stratification induced amplification of the scattering is an approximately linear function of S, say $1 + \beta S$. The dashed line fitted to the points has a slope of $\beta = 2.01$. Symbols correspond to the topographies of: ×, Fig. 4c; ○, Fig. 4a; +, Fig. 4b; *, Fig. 4d.

obtained by examining Davis' (1983) Eq. (2.6), from which it is straightforward to show that a departure from shelf-similarity leaves a term on the right hand side of the equation for the streamfunction (ψ) which is not eliminated by a change of coordinates. The term is proportional to the inner product of $\nabla\psi$ and $\nabla \times \mathbf{k}(h/h_{ss})$, where ∇ is the gradient operator, $\mathbf{k}$ is a unit vertical vector, and h_{ss} is the shape the topography would have if the depth profile at the entrance to the scattering region were carried through the width transition in a shelf-similar manner. If the coastline is given by $y = c(x)$ and the location where the shelf reaches a uniform abyssal depth is given by $y = o(x)$, then according to Hsueh's definition the isobaths of a shelf-similar topography follow lines of constant η^* given by

$$\eta^* = \frac{y - c(x)}{o(x) - c(x)}. \quad (9)$$

Therefore,

$$h_{ss}(\eta^*(x, y)) = h(\eta^*(0, y)). \quad (10)$$

Strictly speaking, $\nabla\psi$ cannot be determined without solving for the CTW flow-field. However, for the purposes of this discussion, and in order to determine an a priori estimate of the scattering induced by a given topography, the following proxy for $\nabla\psi$ is suggested. The vector $\nabla\psi$ is dominated by its across-shelf component which is simply the alongshelf transport, and since the alongshelf transport for a free BSW generally takes a maximum where the across-shelf slope is greatest, a suitable proxy for $(\nabla\psi)_{\text{across-shelf}}$ is $\partial h/\partial s_{\eta^*}$ where s_{η^*} is a coordinate with dimensions of length in the

direction of η^*. Having made this assumption, the magnitude of the term $\nabla\psi \cdot \nabla \times \mathbf{k}(h/h_{ss})$ is approximated by

$$\frac{\partial h}{\partial s_{\eta^*}} \frac{\partial}{\partial s_{\xi^*}} \left(\frac{h}{h_{ss}}\right) \tag{11}$$

where s_{ξ^*} is an 'across-shelf' coordinate perpendicular to s_{η^*}. Since h_{ss} is a function of η^* only, $[\partial/\partial s_{\xi^*}(1/h_{ss})] = 0$, and the quantity in (11) can be integrated over the region of variable topography to give an estimate of the warp factor, F_w:

$$F_w = \int_x \int_{\eta^*=0}^{1} \frac{\partial h}{\partial s_{\eta^*}} \frac{1}{h_{ss}} \frac{\partial h}{\partial s_{\xi^*}} d\eta^* dx. \tag{12}$$

Note that this formulation is consistent with the result that scattering is not sensitive to the alongshelf length of the scattering region. If the length of the region of topographic change doubles, the warp factor is unaltered because any decrease in $\partial h/\partial s_{\xi^*}$ is compensated by an increase in the alongshelf length of the domain of integration.

Evaluating the warp factor F_w for the four narrowing shelf topographies considered above gives the values 0, 1.71×10^{-2}, 3.27×10^{-2} and 3.99×10^{-2}. To examine how the function $W(h)$ depends on F_w, the values of $C_{sc}/(1 + \beta S)$ for each topography are plotted against the corresponding warp factor in Fig. 6. The points fall close to a single straight line suggesting that $W(h)$ is an approximately linear function of F_w, say $W(h) = \alpha F_w$. The straight line passing through the origin which best fits the data in Fig. 6 has a slope of $\alpha = 3.76$.

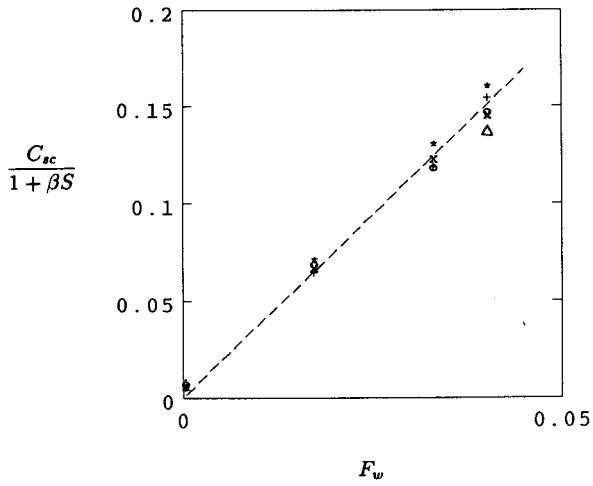

FIG. 6. Scattering coefficient C_{sc}, normalized by $1 + \beta S$, for the four narrowing shelf topographies vs topographic warp factor F_w computed from Eq. (12). This is equivalent to plotting the function $W(h)$ [see Eq. (8)] and shows that $W(h)$ is an approximately linear function of F_w, say αF_w. The dashed line fitted to the points has slope $\alpha = 3.76$. Symbols correspond to different stratifications: ×, $N^2 = 0$; +, $N^2 = 9 \times 10^{-7}$ (and 1.8×10^{-6}); ∗, 2.7×10^{-6}; O, 5.4×10^{-6}; △, 1×10^{-5}.

TABLE 5. Energy fluxes of the transmitted modes generated when a mode 1 incident wave with frequency 1×10^{-5} s^{-1} encounters the widening topography which is the reverse of Fig. 4b for different values of the stratification (N^2). Table entries are calculated in the same manner as Table 1.

	N^2 (s^{-2})				
Mode	0	9×10^{-7}	2.7×10^{-6}	5.4×10^{-6}	1×10^{-5}
1	0.848	0.858	0.831	0.791	0.744
2	0.121	0.137	0.164	0.197	0.240
3	0.030	2.1×10^{-3}	1.0×10^{-3}	8.7×10^{-3}	0.010
4	—	3.0×10^{-3}	4.7×10^{-3}	3.4×10^{-3}	6.5×10^{-3}
	(1.040)	(1.041)	(1.048)	(1.056)	(0.949)

This discussion of the (rather arbitrarily defined) scattering coefficient, though somewhat speculative, has proven useful for synthesizing the results of the narrowing shelf scattering simulations. It is now apparent that topography and stratification act largely independently in the CTW scattering process. Stratification amplifies, by a simple linear gain, the scattering induced by topographic variations which in turn can be related to a topographic warp factor that estimates the degree to which the topography departs from shelf-similarity. A fairly simple empirical relationship for the scattering coefficient C_{sc} has been derived:

$$C_{sc} = \alpha F_w(1 + \beta S) = 3.76 F_w(1 + 2.01S). \tag{13}$$

In principle, the parameters S and F_w can be computed for any narrowing shelf geometry of interest and (13) used to predict the proportion of the energy flux of an incident mode 1 wave which will be scattered into higher modes. The success of the warp factor analysis is encouraging and suggests that a more rigorous examination of the effects of deviations from shelf-similarity may prove to be a fruitful direction for future analytical studies.

c. *Widening shelf results*

Two series of scattering simulations have been conducted to examine how topographic variations and stratification affect CTW scattering on widening shelves. The first series of simulations examines the scattering of CTWs by a widening topography which is simply a reversal of the narrowing shelf topography shown in Fig. 4b. The energy fluxes of the transmitted modes, for an incident mode 1 wave with frequency 1×10^{-5} s^{-1}, are presented in Table 5. Comparison with Table 2 shows that the scattering induced by this widening topography is similar in strength to that induced by the "reciprocal" narrowing topography. In this example, the shelf width increases by a factor of approximately 1.6. In contrast, Wilkin and Chapman (1987) found that an abrupt width change of this magnitude scattered approximately 40% of the energy flux of a mode 1 incident BSW into higher modes. However,

the geometry of the problem considered by Wilkin and Chapman (1987) includes a substantial change in the depth at the coast. Given the tendency of low-frequency flow to follow isobaths, this depth change alone is likely to contribute significantly to the strength of the scattering. It may be expected then, that the more realistic topographic variation of the present numerical experiment would be somewhat less conducive to CTW scattering.

With the exception of the modal energy fluxes for the barotropic case, the results in Table 5 exhibit the same trend observed in the narrowing shelf experiments; scattering is amplified by stratification. In Fig. 7, the scattering coefficient C_{sc} for each of the runs in Table 5, normalized by the zero stratification value, is plotted versus Burger number (S). Except for the zero stratification result, the points fall close to a line with the same slope as the function $1 + \beta S$ (shown by the dashed line) fitted to the narrowing shelf results (Fig. 5). The departure of the barotropic result from the simple functional form for the scattering coefficient postulated in equation (8) is possibly due to the fact that in the barotropic limit transmitted mode 3 is very close to being evanescent at this frequency. Wilkin and Chapman (1987) found that local minima occur in the energy flux of transmitted mode 1 near parameter values at which higher transmitted modes become evanescent. It may be, then, that the low value of the energy flux in transmitted mode 1 for this topography and zero stratification results from the anomalously high value obtained for the nearly evanescent mode 3.

The second series of simulations considers CTW scattering at a fixed stratification of $N^2 = 5.4 \times 10^{-6}$ s^{-2} for several different widening shelf topographies; namely, those obtained when the topographies of Figs. 4a through 4d are reversed. The energy fluxes of the

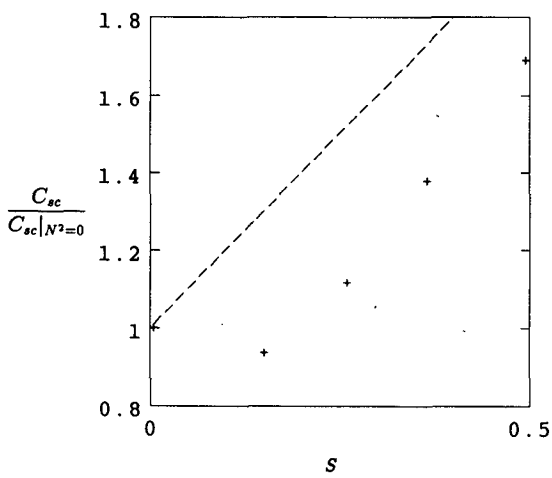

FIG. 7. Scattering coefficient C_{sc} values for the widening topography which is the reverse of Fig. 4b, normalized by $C_{sc|N^2=0}$, vs Burger number $S = NH/fL$. The dashed line is the function $1 + \beta S$ fitted to the narrowing shelf results (Fig. 5).

TABLE 6. Energy fluxes of the transmitted modes generated when a mode 1 incident wave with frequency 1×10^{-5} s^{-1} encounters different widening shelf geometries; namely, those obtained by reversing the topographies of: Fig. 4c (column A), Fig. 4a (column B), Fig. 4b (column C), and Fig. 4d (column D). The columns are arranged left to right in order of increasing departure from shelf-similarity. The topographic warp factors for these topographies are 0, 7.81×10^{-3}, 7.85×10^{-3} and 9.82×10^{-3} for A through D, respectively. For all cases the stratification is $N^2 = 5.4 \times 10^{-6}$ s^{-2}.

	Topography			
Mode	A	B	C	D
1	0.979	0.867	0.791	0.757
2	0.011	0.132	0.197	0.238
3	7.0×10^{-3}	1.2×10^{-3}	8.7×10^{-3}	4.1×10^{-3}
4	2.6×10^{-3}	2.7×10^{-4}	3.4×10^{-3}	1.1×10^{-3}
	(1.099)	(1.098)	(1.056)	(1.044)

scattered modes are presented in Table 6 with the columns arranged left to right in order of increasing departure from shelf-similarity. The same trend observed in the narrowing shelf experiments is evident; scattering strength increases with increasing departure from shelf-similarity.

Comparison of the values in Table 6 with the corresponding entries in Tables 1 through 4 shows that, overall, the strength of the scattering for each widening topography is quite similar to that observed for its reciprocal narrowing topography. For example, the transmitted mode 1 energy fluxes for the narrowing shelf topographies for $N^2 = 5.4 \times 10^{-6}$ s^{-2} are, in order of increasing nonshelf-similarity: 0.988, 0.877, 0.795 and 0.746, which are close to the reciprocal widening shelf values in row 1 of Table 6.

The topographic warp factors F_w for these widening topographies are 0, 7.81×10^{-3}, 7.85×10^{-3} and 9.82×10^{-3}. In a plot analogous to Fig. 6 (for narrowing shelves), Fig. 8 shows $C_{sc}/(1 + \beta S)$ plotted versus F_w. In the normalization $\beta = 2.01$ was used since the results of the last series of experiments suggest that the value of β determined from the narrowing shelf experiments is valid for widening shelves also. The points plotted do not cluster as closely to a single straight line as they did for the narrowing shelf scattering simulations. Furthermore, the slope of a straight line fitted to these widening shelf results differs by a factor of roughly 3.5 from the slope of the line fitted to the narrowing shelf results. Therefore, while it is clear that scattering strength is related to the simple definition of warp factor proposed in (12), some refinements to the definition are required before it can be applied reliably to the prediction of the strength of CTW scattering on continental shelves of practical interest.

d. Flow field near the scattering region

Discussion thus far has concentrated on the gross scattering effects of irregular coastal geometry; namely,

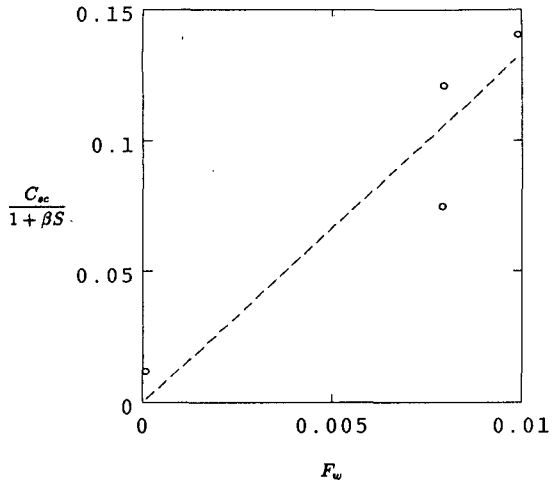

FIG. 8. Scattering coefficient C_{sc}, normalized by $1 + \beta S$, for the widening shelf results of Table 6 vs topographic warp factor F_w computed from Eq. (12). The value of β used is that determined from the narrowing shelf experiments (Fig. 5). The dashed line fitted to the points has a slope of 13.3.

the amplitudes of the transmitted modes which propagate freely away from an isolated scattering region. A comparison of narrowing and widening topographies showed that the amplitudes of the freely propagating transmitted modes generated by "reciprocal" narrowing and widening topographies are quite similar. However, significant differences are found in the scattering effects of narrowing and widening geometries when the flow fields close to the topographic variation are examined.

1) WIDENING SHELVES

The BSWs propagating through the widening shelf geometry considered by Wilkin and Chapman (1987) were found to leave a shadow zone of weak flow behind the coastline bend. This occurs because low-frequency flow has a tendency to follow f/h contours (isobaths on an f-plane) and therefore requires a finite alongshelf distance to adjust to the changing depth at the coast. More realistic idealizations of irregular shelf topography, such as those considered in the present numerical experiments, have a depth at the coast which does not vary appreciably alongshelf, and is small relative to the deep-ocean depth. The question arises, then, as to whether or not a shadow zone would occur on more realistic shelves. This is addressed by examining the scattered wave flow field in the vicinity of the topographic and coastline variation for some of the widening shelf model runs.

Figure 9 shows a sequence of plots of surface velocity vectors at different times during one wave period, for the case of a mode 1 incident CTW with frequency $1 \times 10^{-5}\ \mathrm{s}^{-1}$ propagating through the widening topography which is the reverse of Fig. 4b, for $N^2 = 5.4 \times 10^{-6}\ \mathrm{s}^{-2}$. The transmitted wave energies for this case are shown in the fourth column of Table 5. Note that the across-shelf scale in Fig. 9 has been expanded for clarity, and that only the vectors at every third alongshelf grid point and every second across-shelf grid point of the numerical model are plotted. The topography is also shown (with the correct aspect ratio of horizontal scales). Figure 10 shows the sequence of plots of the locally alongshelf component of the surface velocity corresponding to Fig. 9, along with a plot of the coordinate grid used in the simulation (with the correct aspect ratio of horizontal scales). The "alongshelf" velocity component is in the direction of the ξ computational coordinate.

In the first frame of Figs. 9 and 10, a crest of the mode 1 incident wave is approaching from the left. In the next two frames the crest reaches the region of varying topography and the subsequent scattering produces considerable variation in the velocity field over short spatial scales. A cell of intense alongshelf flow trapped close to the inflection in the coastline is particularly evident in frame 3. The fourth frame corresponds to the time at which the amplitude of transmitted mode 1 is almost zero at the location where the mode fit is performed (indicated by the single tick marks). Consequently, the flow there is dominated by the signature of transmitted mode 2, i.e., there are two zero crossings in the across-shelf structure of the alongshelf velocity at this time (Fig. 10). In frame 5 an intense coastal return flow occurs in the scattering region as the trough of the incident wave reaches the coastline bend.

A more detailed picture of the time variation of the coastal currents is shown in Fig. 11, where the alongshelf velocity at the coast is plotted as a function of alongshelf coordinate ξ, and time t, for the entire duration of the simulation. Each line across the field of view corresponds to a snapshot of the coastal alongshelf velocity. A section through the plot, into the background, gives a time series of the velocity at a particular coastal location.

At the beginning of the simulation (i.e., the foreground of the plot) the numerical wavetank is quiescent. As time advances (into the background) the amplitude of the wavemaker increases over one wave period, and then oscillates with fixed amplitude for two additional wave periods. Following the first crest of the wavetrain through the coastline bend, the wave-induced current first diminishes, then increases abruptly, and then drops to almost zero before the scattered waves emerge from the scattering region. This pattern is fully established once the second wave crest has passed through the scattering region. The sequence of peaks in Fig. 11 emphasizes the intense current events associated with the passage of each wave, while the saddles indicate the zones of weak flow.

While there is a region of weak coastal flow immediately downstream from the coastline bend, this is not

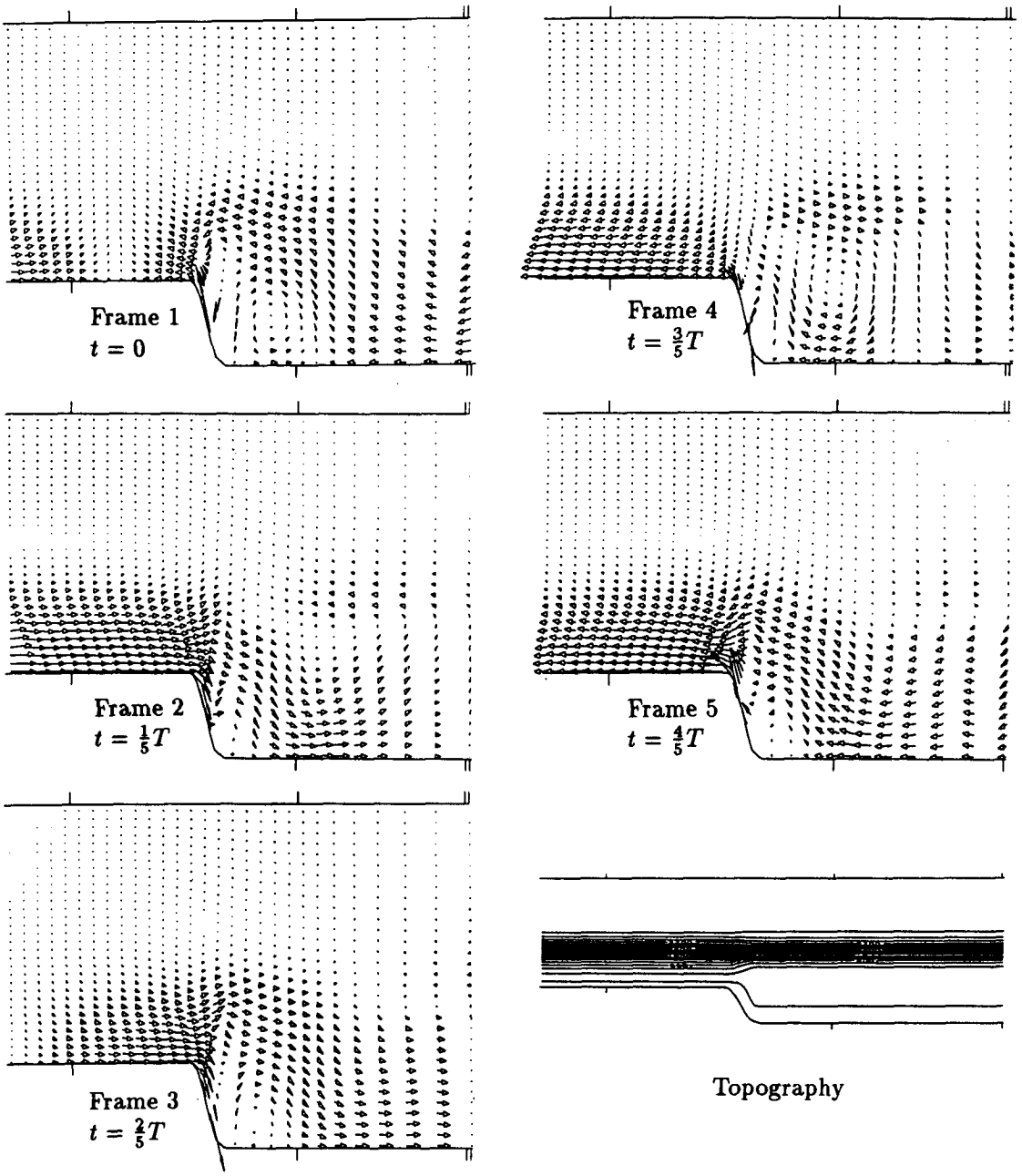

FIG. 9. A sequence of plots of surface velocity vectors at different times t during a single wave period (T). The case shown is a mode 1 incident CTW with frequency 1×10^{-5} s^{-1} propagating through the widening topography which is the reverse of Fig. 4b. $N^2 = 5.4 \times 10^{-6}$ s^{-2}. The transmitted energy fluxes for this case are shown in column 4 of Table 5. Note that the across-shelf scale has been expanded for clarity and that only the vectors for every third alongshelf and every second across-shelf grid point of the numerical model are shown. The topography is shown with the correct aspect ratio of alongshelf and across-shelf scales.

the signature of a shadow zone. The existence of a shadow zone would be indicated by weak currents throughout the scattering region, whereas here it is found that within the scattering region intense coastal currents occur which exceed in strength those of the incident wave. Farther downstream the pattern is qualitatively similar to the analytical results of Wilkin and Chapman (1987)—the interaction of multiple transmitted waves with different wavelengths modulates the flow field. Note that it takes two to three wave periods for the downstream flow field to become truly periodic. This is due to the slower propagation speeds

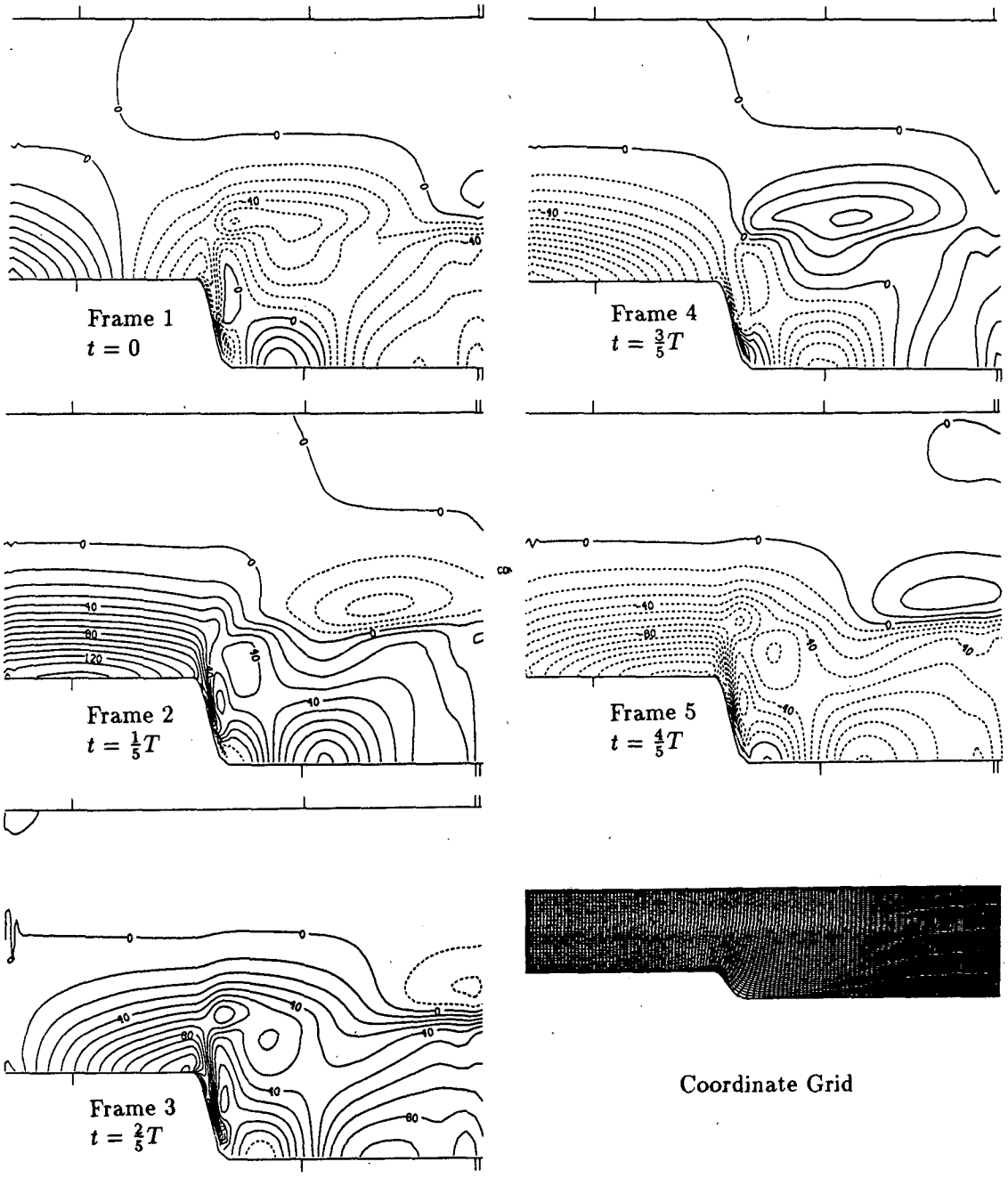

FIG. 10. A sequence of plots of the surface alongshelf velocity (i.e., velocity in the direction of the ξ computational coordinate) for the same case shown in Fig. 9. The coordinate grid used in the simulation is shown with the correct aspect ratio.

of transmitted modes 2 and 3. The straight ridges of constant amplitude "upstream" from the scattering region in Fig. 11 show that there is no reflection.

In Fig. 12, a comparison is made of these wave-induced coastal currents to those generated by the other widening shelf geometries considered in section 3c. The figure shows the maximum alongshelf velocity at each location along the coast, normalized by the maximum coastal velocity of the incident wave. The curves are labeled A through D to correspond with the columns of Table 6. Curve C is therefore the "envelope" of the oscillatory currents depicted in Fig. 11. The origin of the alongshelf coordinate is the beginning of the scattering region, which is 100 km long for cases A, C and D, and 200 km long for case B.

Cases B and D each exhibit a shadow zone qualitatively similar to that obtained by Wilkin and Chapman (1987). In both cases the width of the continental

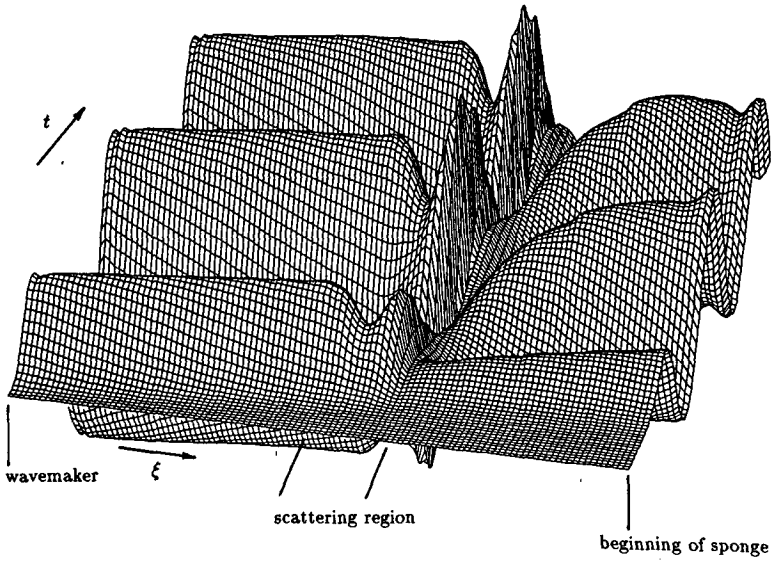

FIG. 11. Surface alongshelf velocity at the coast, through time, for the entire duration of the same numerical experiment shown in Figs. 9 and 10. Each line across the field of view corresponds to a snapshot of the coastal alongshelf velocity. A section through the plot, into the background, gives a time series of the velocity at a particular coastal location.

shelf increases rapidly in the scattering region and it is tempting to invoke the "flow-following-isobaths" mechanism as an explanation for the presence of a shadow zone. However, the shelf depth profiles outside the scattering region in case D are identical to those in case C—the difference in the two topographies being limited to the shape of the coast. The markedly different response within the scattering region for these two cases demonstrates that the scattering process active here is more complex than that proposed to explain the results of Wilkin and Chapman (1987).

Of particular interest is case A—the shelf-similar

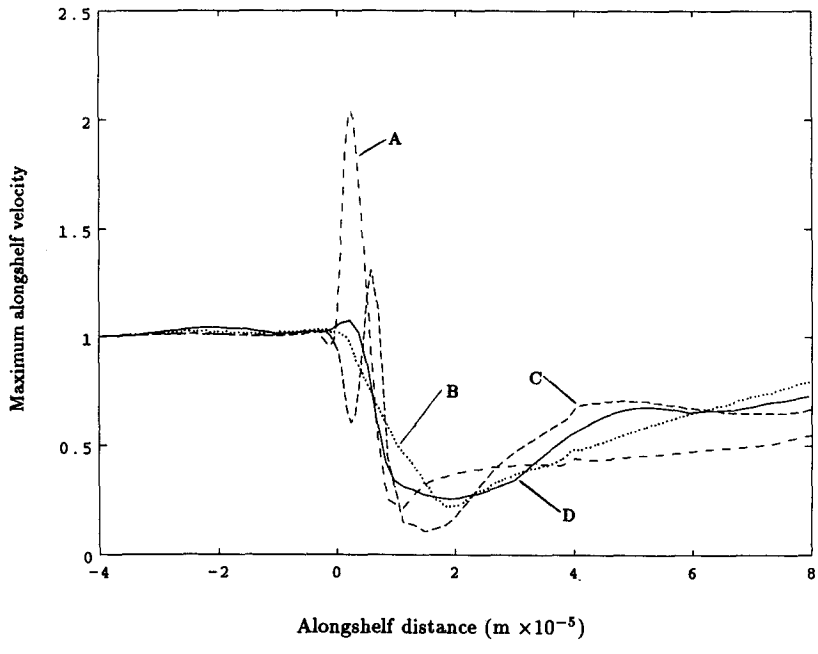

FIG. 12. Maximum alongshelf velocity at the coast for the four widening shelf geometries considered in Table 6. Labels A through D correspond to the columns of Table 6.

widening topography. For this topography the incident mode 1 wave emerges from the scattering region without any appreciable loss of energy (Table 6). It might have been expected, then, that the flow would exhibit a smooth transition from the across-shelf structure of mode 1 on the incident side to that of mode 1 on the transmitted side. In actuality, there is a strong intensification of the coastal velocity immediately following the start of the coastline bend, and an equally significant decrease in the coastal flow shortly thereafter. Since in this case there is no reflection, and the amplitudes of the scattered waves are very small, the strong spatial modulation of the flow within the region of variable topography must be due to non-propagating (i.e., evanescent) flow structures excited within the scattering region.

2) Narrowing shelves

Examination of the narrowing shelf model runs provides further evidence that evanescent wavelike motions contribute significantly to the flow field induced by CTWs near regions of variable topography. Figure 13 shows a sequence of plots of surface velocity vectors at different times during a wave period, for the case of a mode 1 incident CTW encountering the topography of Fig. 4b, for $N^2 = 5.4 \times 10^{-6}\ \mathrm{s}^{-2}$. The transmitted wave energies for this case are shown in column 4 of Table 2. As in the widening shelf example, there are regions within the area of changing topography where the wave-induced currents are amplified significantly. It is also evident, particularly in frames 3 and 5, that the directions of the wave-induced currents vary considerably over short spatial scales, indicating the possibility of rapid phase changes.

A feature not observed in the widening shelf example is a noticeable upstream influence by the scattered wave field on the incident-wave flow. The across-shelf component of the currents associated with the long incident wave is weak, and as a result the velocity vectors in the region well to the left of the scattering region in each frame of Fig. 13 are aligned almost exactly alongshelf. However, near to the scattering region, perturbations to this solely alongshelf flow are evident (frames 1, 3 and 4). This indicates that the scattering has introduced an appreciable across-shelf component to the CTW flow field near to, yet still upstream from, an abrupt narrowing of the continental shelf. This occurs despite the stratification being sufficiently strong to eliminate any possibility of propagating reflected CTWs (i.e., $\omega < \omega_{\infty,\,\mathrm{wide}}$).

The alongshelf structure of this upstream influence can be seen in Fig. 14, which shows the alongshelf velocity at the coast, through time, in the same manner as Fig. 11. Immediately upstream from the coastline bend, the coastal currents exhibit characteristics of an evanescent wave mode; namely, the envelope of the current fluctuations has a sinusoidal alongshelf structure which decays exponentially away from the scattering region. The wavelength and alongshelf decay scale of this evanescent mode can be estimated from curve C of Fig. 15, which shows the maximum alongshelf velocity at the coast. The mode decays over roughly 200 km, and the two local maxima within this region indicate a wavelength of roughly 100 km.

Figure 15 includes the maximum alongshelf velocities for the other three narrowing shelf topographies studied, for $N^2 = 5.4 \times 10^{-6}\ \mathrm{s}^{-2}$. Cases A, B and D correspond to the topographies of Figs. 4c, 4a and 4d, respectively, and exhibit patterns qualitatively similar to case C. In all cases there is evidence of an evanescent mode influencing the flow field upstream from the scattering region. Furthermore, in all cases except A (shelf-similar), the coastal currents near the inflection in the coast exceed those outside the scattering region. In case A, the maximum coastal currents actually occur some 50 km upstream from the scattering region.

4. Scattering along the East Australian Coast: A case study

The results of the numerical experiments show that large irregularities in coastline and topography cause appreciable scattering of CTW energy into modes other than that of the incident wave. The generation of multiple transmitted modes with differing across-shelf structures and propagation speeds produces an alongshelf modulation of the wave-induced flow field which may be important observationally. Also of likely significance to observational studies are the intensification and the increase in spatial variability of the wave-induced currents within the scattering region of many of the irregular coastal geometries considered in the numerical experiments.

It was noted by Wilkin and Chapman (1987) that some qualitative features of their solution have been seen in the observations made by Griffin and Middleton (1986, hereafter referred to as GM) on the East Coast of Australia. In this section, the study by GM is discussed further in light of the results of section 3, and by examining the results of a numerical wavetank simulation of the scattering of a CTW pulse by coastal geometry which approximates closely the geography of the GM study site.

Griffin and Middleton reported observations of sea level, current, and temperature at three across-shelf sections between Fraser Island (FI) and the southern end of the Great Barrier Reef (Fig. 16). They concluded that local wind-driving could not account for the substantial energy observed at subinertial frequencies and that, instead, the observed low-frequency currents were due principally to waves which propagated into the study region from south of FI. Evidence for the presence of freely-propagating CTWs within the study region comes from a modal decomposition of the across-shelf structures of the alongshelf currents at the central

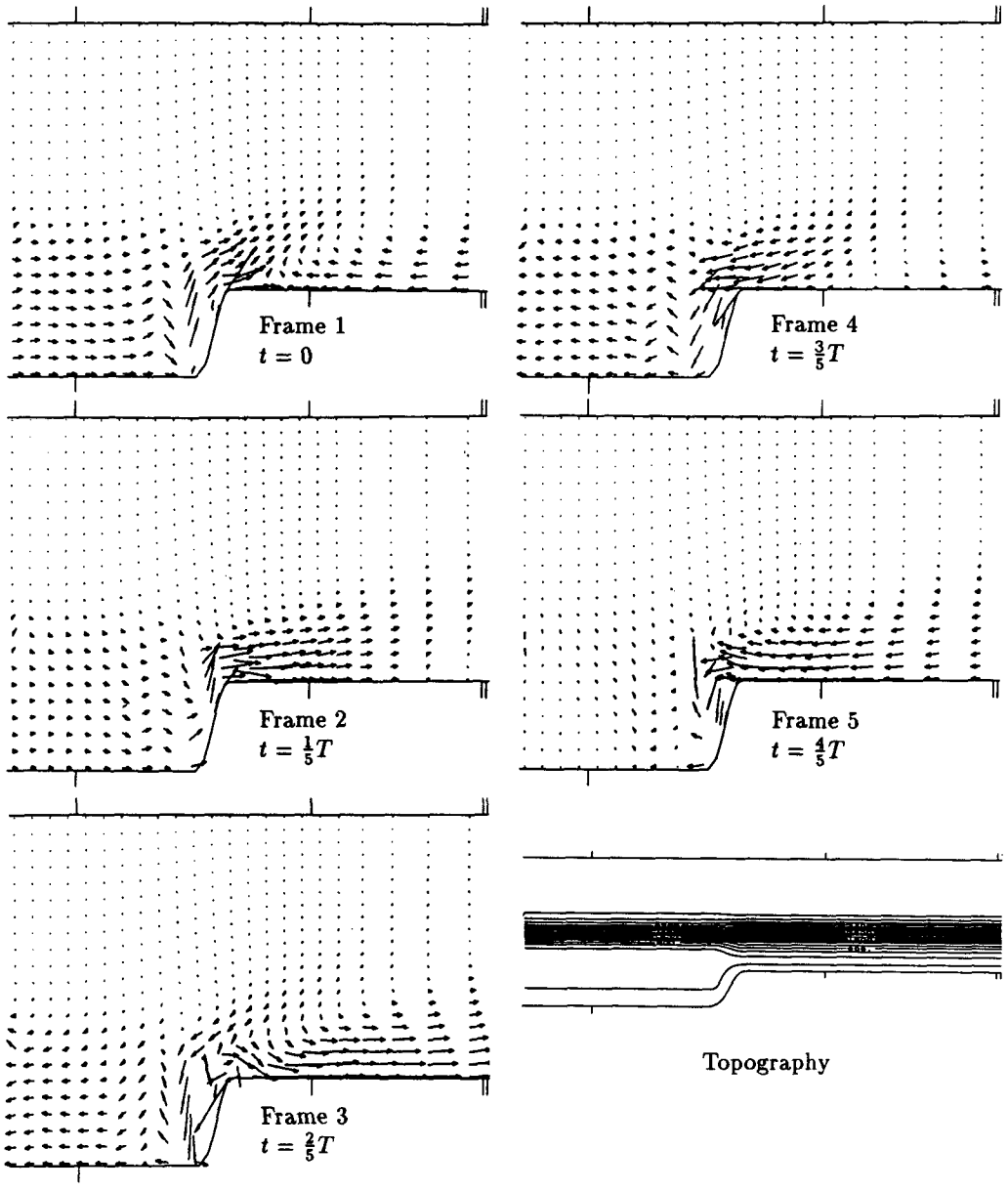

FIG. 13. A sequence of plots of the surface velocity vectors at different times during a single wave period. The case shown is a mode 1 incident CTW with frequency $1 \times 10^{-5}\ s^{-1}$ propagating through the topography of Fig. 4b. $N^2 = 5.4 \times 10^{-6}\ s^{-2}$. The transmitted energy fluxes for this case are shown in column 4 of Table 2. Note that the across-shelf scale has been expanded for clarity. The topography is shown with the correct aspect ratio.

instrument line. Using the fitted mode amplitudes, currents at the southern current-meter site were hindcast by propagating the modes at their predicted phase speeds. Good agreement between the observed and hindcast currents suggested strongly that freely propagating CTWs account for much of the subinertial frequency variability within the study region. The modal decomposition indicated that the majority of the energy was carried by a second or third mode CTW having a period of approximately 9 days, and a propagation speed of about 0.4 m s^{-1}. Evidence that there is a source for these waves in the form of freely-propagating CTWs incident upon FI may be found in the results of the Australian Coastal Experiment (ACE) (Freeland et al. 1986), which in part ran concurrently with GM's field study. The ACE results showed the presence of CTWs on the continental shelf between 400 and 1000 km south of FI, and since the shelf topography between FI and Evans Head (the northernmost ACE instrument line) is only slowly varying, it is probable that free CTWs were incident upon FI during GM's instrument deployment. Griffin and Middleton established a con-

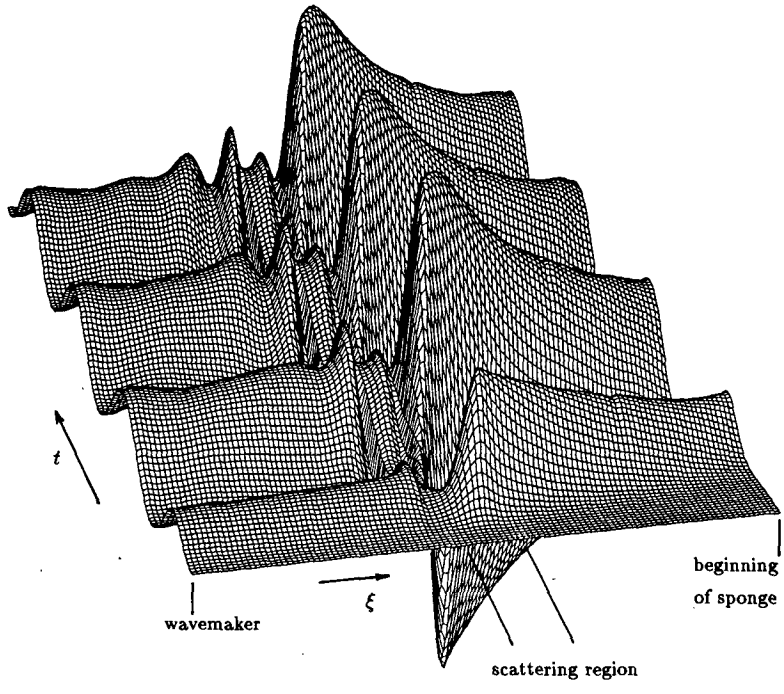

FIG. 14. Surface alongshelf velocity at the coast, through time, for the entire duration of the same numerical experiment shown in Fig. 13. Each line across the field of view corresponds to a snapshot of the coastal alongshelf velocity. A section through the plot, into the background, gives a time series of the velocity at a particular coastal location.

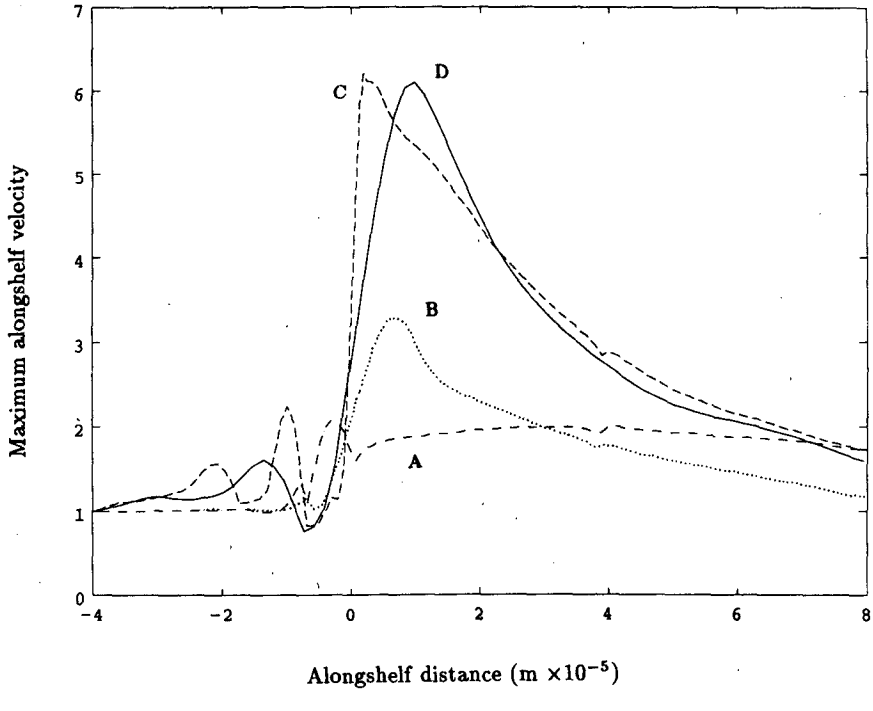

FIG. 15. Maximum alongshelf velocity at the coast for the four narrowing shelf geometries considered in section 3b. Labels correspond to the $N^2 = 5.4 \times 10^{-6}\ \mathrm{s}^{-2}$ runs of the following topographies: A, Fig. 4c; B, Fig. 4a; C, Fig. 4b; D, Fig. 4d.

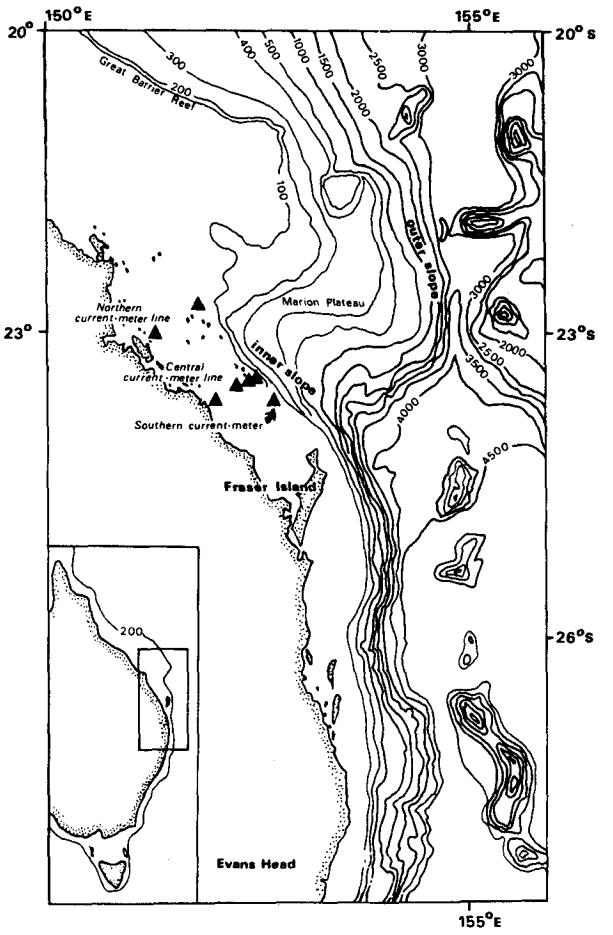

FIG. 16. The region of the East Coast of Australia where observations by Griffin and Middleton (1986) reveal the presence of scattered CTWs. The sites where current meters were deployed by GM are indicated by the solid triangles.

nection between these incident waves and the CTWs they observed by demonstrating that there is a statistically significant lagged correlation between the currents at Evans Head and the currents north of FI. The phase difference GM computed was 33 hours, which corresponds to a northward propagation speed of approximately 4.5 m s^{-1}.

Our results in section 3 provide additional support for GM's conjecture that free waves incident from south of FI would be scattered by the irregular topography of the region and thereby generate the waves observed in their data. The geography of the FI region is comprised of features which resemble some of the topographic irregularities considered in isolation in section 3. Approaching FI from the south, the shelf width decreases to a narrow neck adjacent to the northern tip of FI (Fig. 16). This narrowing is similar in some respects to the topography of Fig. 4a, which scattered up to 13% of an incident mode 1 CTW into higher modes (Table 1) and produced an intensification in the alongshelf currents at the narrowest part of the scattering region (Fig. 15, curve B). To the north of FI, the shelf widens rapidly and the isobaths essentially split to form two "slopes." The shelf and inner slope, where GM's instruments were deployed, are separated from the outer slope by the Marion Plateau, which is fairly uniform in depth (~450 m) across its 200 km width (Fig. 16). The isobaths of the outer slope move offshore in a manner similar to the least shelf-similar widening topography considered in section 3 (i.e., the reversal of the topography of Fig. 4d), which scattered over 20% of the incident wave energy (Table 6, column D). The topography of the inner slope and shelf is more analogous to that used in the first series of widening shelf scattering experiments (Table 6, column C) where the shallow inner shelf widens due principally to a change in the position of the coast. Considered in isolation in section 3, each of these topographic variations caused appreciable scattering of CTW energy, and a significant modulation of the flow field both within, and immediately downstream from, the scattering region. This suggests that it is indeed likely that free waves encountering the irregular geometry of the FI region would produce an observable signal, in the form of freely propagating scattered CTWs, on the inner slope and shelf north of FI.

To test this hypothesis more rigorously, a numerical wavetank experiment was conducted which simulates the scattering of a free CTW pulse by a model topography (shown in Fig. 21) which approximates closely the geography of the FI region. Comparison of the model topography with Fig. 16 shows that the model topography is somewhat smoother than the actual topography of the region, and that an arbitrary abyssal depth of 3000 m was chosen. It was necessary to model the promontory of FI as a rather blunt peninsula in order to avoid prohibitively small spacings in the computational coordinate grid. Apart from this approximation, the model geometry closely follows that of the FI region. South of FI, and north of the Marion Plateau, the topography has been extended uniformly alongshelf. This makes it possible to limit the scattering observed in the simulation to that generated solely by the geography of the FI region. Church et al. (1986a) observed N^2 values of roughly 5×10^{-6} s^{-2} below 500 m depth in the ACE region. This value, assumed constant throughout the water column, was adopted for the FI simulation. The shallow thermocline (~100 m depth) observed by GM in their CTD casts over the Marion Plateau was not included in the simulation due to difficulties that the PEM has resolving such a near-surface feature in the deepest regions of the computational domain. The omission of the thermocline has negligible effect on the free wave dispersion relations (results not shown) but does create some differences in the details of the modal structures which are discussed later.

The choice of an appropriate input for the simulation is not straightforward. GM noted a peak in the subinertial frequency spectra of their observations at

around 9 days. However, during those periods of the instrument deployment which were dominated by energy in the 6–10 day frequency band, the observed currents had a nonzero northward mean, and therefore could not be simply the signature of a continuous train of CTWs. This could be due to the presence of a northward mean flow unrelated to the CTWs, or to the observed waves being essentially nondispersive CTW pulses with predominantly northward alongshelf current signatures. For the purposes of this discussion it was assumed that the latter was the case, and a single mode 1 CTW pulse representing the crest of a 9-day-period CTW was chosen as the input to the simulation. A mode 1 input wave was assumed because the phase speed of mode 1 (3.44 m s^{-1}) most closely corresponds to the observed speed (4.5 m s^{-1}) at which current fluctuations propagated into the study region from Evans Head. At this frequency ($0.13f$) the CTWs are only weakly dispersive (results not shown) so the amplitudes of the modes scattered by a pulse should not differ significantly from those generated by a continuous wavetrain (Wilkin and Chapman 1987). The results should therefore be similar qualitatively to those which would be obtained for other input waveforms.

The output of the simulation was analysed in the same manner as the results of the previous numerical experiments, i.e., by performing a fit of the calculated alongshelf currents to a set of freely-propagating scattered CTW modes. The alongshelf location at which the mode fit was performed (indicated by the single tick marks in Fig. 21) was chosen to correspond to the location of GM's central instrument line. Performing the mode fit at such a location, i.e., where the topography is changing alongshelf, is not strictly valid because the assumption that the local CTW modes have a simple-harmonic alongshelf dependence (section 2) cannot be made. Nevertheless, the analysis was performed in this manner to facilitate as direct a comparison as possible to the modes which GM fitted to their observations. Computation of the free-wave modal structures and phase speeds at this location reveals some interesting properties of the 'dual slope' topography north of FI. The across-shelf structures of the first six modes are shown in Fig. 17. The structure of mode 1 takes a maximum at the coast, decays slightly over the inner slope, remains relatively constant over the Marion Plateau, and does not take its zero crossing until over the outer slope. The structures of the higher

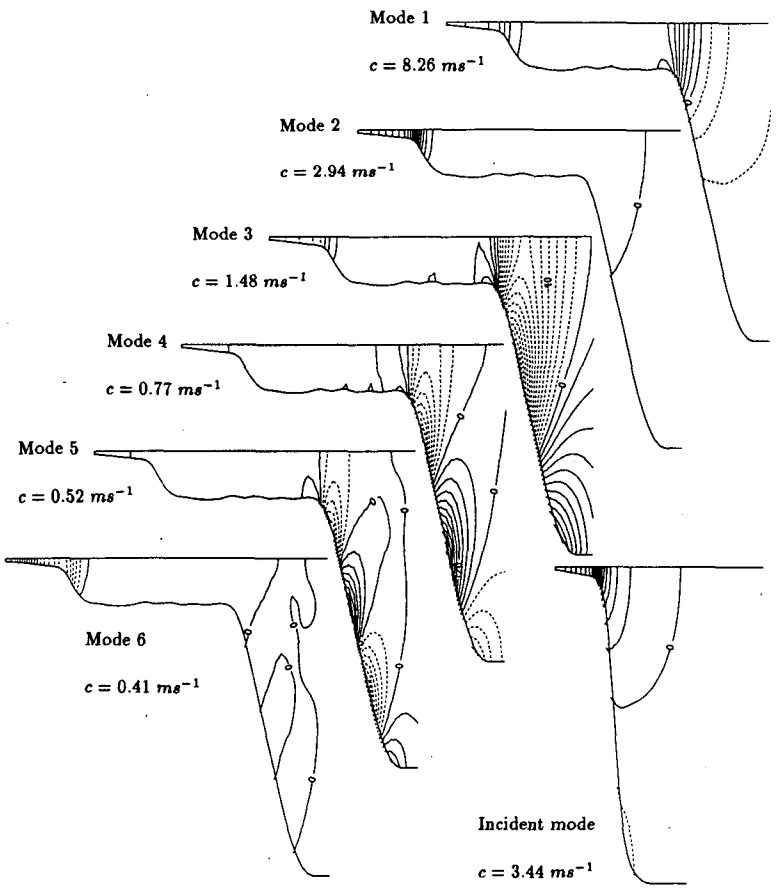

FIG. 17. Across-shelf modal structures of the incident wave (mode 1) and the first six transmitted modes. The alongshelf location at which the transmitted modes were computed is indicated by the single tick marks in Fig. 21.

modes fall into two distinct classes: modes 3, 4 and 5 are concentrated over the outer slope, while modes 2 and 6 are trapped closely against the inner shelf and slope. None of these modes has any appreciable signal over the Marion Plateau. Griffin and Middleton calculated their modal structures under the assumption that the wave motions they observed were confined to the inner shelf and slope, and were unaffected by the topography of the outer slope due to the broadness of the Marion Plateau. Their analysis therefore missed those modes (3, 4 and 5) in Fig. 17 whose structures are concentrated over the outer slope. Nevertheless, there appears to be a direct correspondence between GM's modes (GM, their Fig. 8) and the inner slope modes of Fig. 17. In particular, GM's mode 1, which has a phase speed of 3.1 m s^{-1} and a zero crossing at mid-depth on the inner slope, appears to correspond to mode 2 in Fig. 17, which has a phase speed of 2.94 m s^{-1}. Although mode 6 of Fig. 17 has a phase speed of 0.41 m s^{-1}, which is virtually identical to GM's mode 3 (0.4 m s^{-1}), the across-shelf structure of mode 6 resembles that of GM's mode 2, with zero crossings on the shelf and at the foot of the inner slope. This ambiguity is not of particular concern given that GM were unable to distinguish between the contribution of their modes 2 and 3 to the observed currents. Furthermore, the structure of GM's mode 2 was particularly sensitive to the assumed depth of the thermocline (D. Griffin, personal communication) which has been omitted from the simulation.

The time series of the amplitudes of the scattered modes returned by the least-squares mode fit are shown in Fig. 18. It can be seen that the incident wave pulse scatters primarily into two pulses (modes 1 and 2) of similar shape to the incident pulse. The arrival of the first two pulses is followed by a tail of predominantly higher mode waves. These may be the signature of waves generated at the beginning of the region of irregular topography which are scattered repeatedly throughout the finite length of the scattering region, or alternatively, this tail could simply result from the more dispersive nature of the higher mode pulses.

The magnitude of the mode 1 pulse shows that the majority of the incident mode energy remains in mode 1, as was the case in the results of section 3. This raises a question as to why GM did not observe this mode in their data. In Fig. 17 it can be seen that the structures of modes 1 and 2 are quite similar over the inner slope and shelf. Since GM did not have any instruments deployed over the outer slope, where the structures of these modes differ, it is unlikely that their analysis would be able to discriminate between the signals of the two modes. Furthermore, a mode 1 and mode 2 wave generated simultaneously at FI would reach GM's northernmost current meter less than half a day apart—a time separation too small to be resolved by GM's spectral analysis. The strong peak of the mode 2 pulse shows that a significant amount of the scattered energy propagates along the inner slope into GM's study area. The energy in the remaining higher modes is small. In particular, mode 6, which corresponds to GM's mode 2 or 3, carries little of the scattered energy flux. Nevertheless, this mode has a strong signal in the currents on the inner slope and shelf. Figure 19 shows

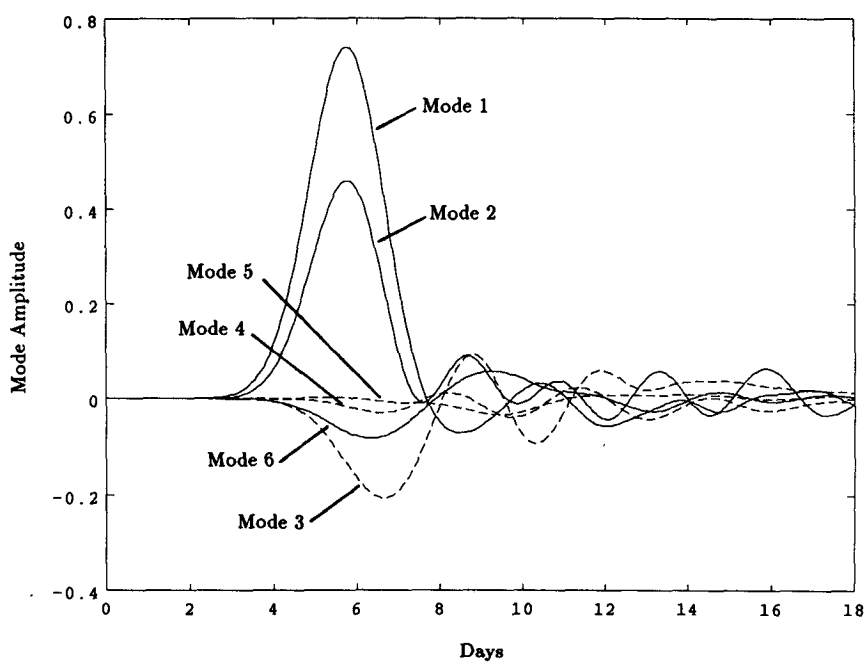

FIG. 18. Time series of the amplitudes of the transmitted modes calculated by the least-squares mode fit for the FI case study simulation.

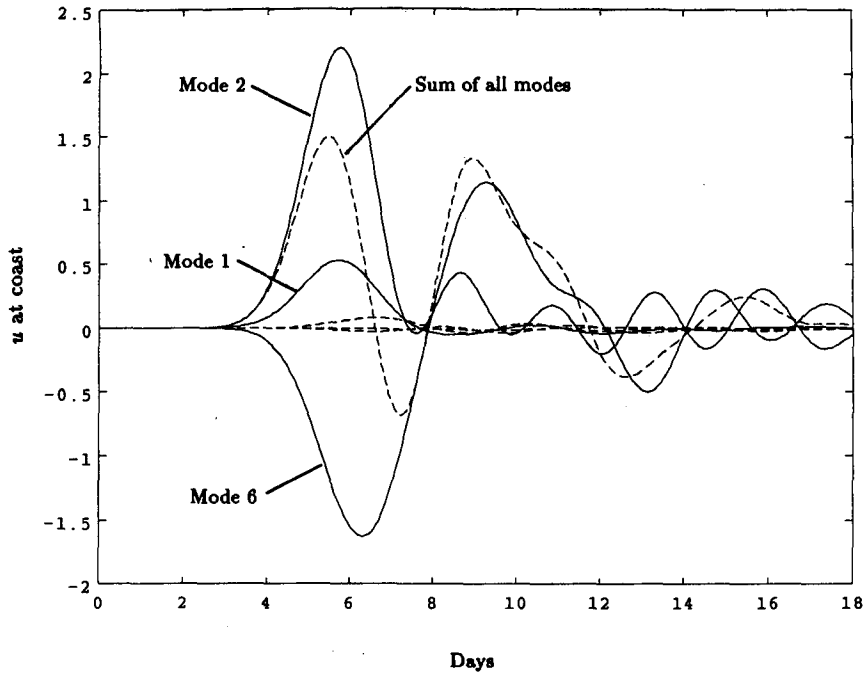

FIG. 19. Surface alongshelf current at the coast at the location corresponding to GM's central instrument line. The current due to each mode is computed by taking the product of the mode amplitude time series (Fig. 18) and the value of the individual modal structures (Fig. 17) at the coast. Dashed line shows the superposition of individual contributions.

the contribution of each mode to the total surface alongshelf velocity at the coast, computed by multiplying the mode amplitude time series (Fig. 18) by the values of the mode structures at the coast. The velocity at the coast due to the energetic mode 1 wave is quite weak, providing a further reason why its signal should not be particularly evident in GM's observations. By far the strongest signals are those due to the inner slope

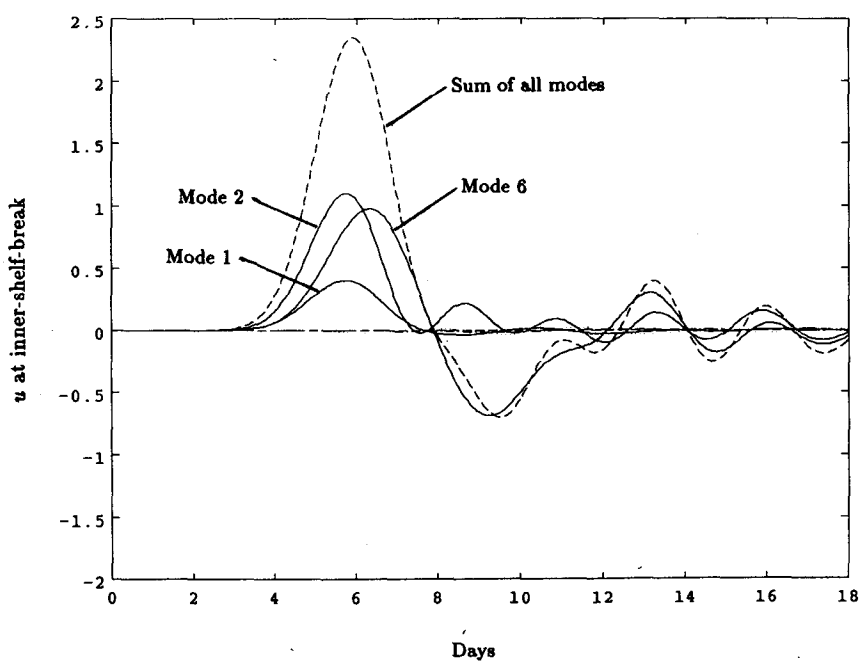

FIG. 20. Surface alongshelf current at the inner shelf break at the location corresponding to GM's central instrument line. The currents are computed in the same manner as Fig. 19.

modes; modes 2 and 6. The phase lag between their arrivals at the mode fit section (~0.5 days) is consistent with the difference in their phase speeds if the waves were generated at the tip of FI. The coastal currents induced by these two modes largely cancel, in agreement with GM's observations that their modes 1 and 2 added in near antiphase near the coast. Conversely, at the inner shelf break the currents induced by the modes reinforce (Fig. 20). This is also in agreement with GM's observations; namely, that the subinertial frequency currents at their central instrument line were most energetic at the shelf-break. This qualitative similarity between the features of the simulation and GM's observations lends strong support to GM's hypothesis that the waves they observed were scattered from freely-propagating CTWs originating south of FI.

Some other interesting features of the simulation may be seen in Fig. 21 which shows the time history

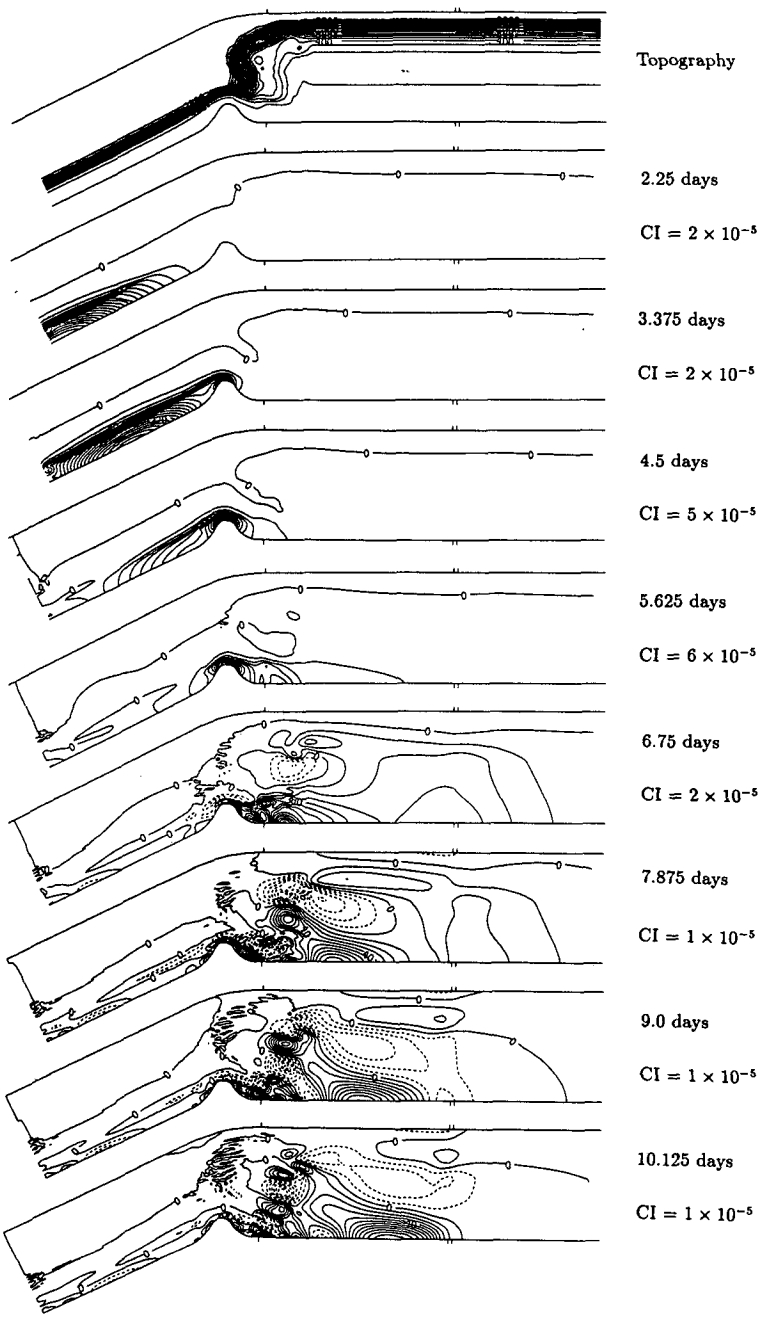

FIG. 21. Surface alongshelf velocity at different times during the FI scattering simulation. CI denotes contour interval. Note that the plots are presented in a reflected "Northern Hemisphere" geometry for comparison with similar figures in section 3.

of the surface alongshelf velocity as the pulse propagates through the scattering region. The figures have been drawn in a "Northern Hemisphere" geometry so that they can be compared with similar plots in section 3. As the pulse reaches the promontory of FI intense alongshelf currents are generated. These achieve a maximum value three times greater than the coastal currents associated with the incident wave (Fig. 22). The separation of the individual pulses as they reach the uniform topography north of the Marion Plateau is also apparent.

5. Summary

Coastal-trapped waves propagate along many of the continental shelves of the world's oceans and can transmit fluctuations in sea level and current over vast distances. Along relatively straight coasts, where the long wave approximation can be made, wind-driven CTW motions have been hindcast with some success by application of the FOWE method which incorporates variations in bottom topography and coastline only through slow alongshelf changes in the wave parameters. However, most coastlines vary significantly over spatial scales much shorter than CTW length scales, thereby introducing the possibility that appreciable scattering of CTW energy from one mode into others can occur over short alongshelf distances.

In this study we have used a numerical model which accomodates arbitrary density stratification, bathymetry, and coastline, to examine how freely propagating CTWs are scattered by large variations in coastline and topography occurring over alongshelf distances comparable to the shelf width in a realistically stratified coastal ocean. The strength of the scattering, as measured by the proportion of the incident energy flux scattered into modes other than that of the incident wave, was found to be proportional to a topographic warp factor which estimates the extent to which the topography departs from shelf-similarity. The scattering induced by nonshelf-similar topographic variations is amplified by density stratification. A comparison of the effects of widening and narrowing topographies showed that the amplitudes of the freely propagating transmitted modes generated by "reciprocal" narrowing and widening topographies are quite similar. Within the scattering region itself, the strengths of the scattered-wave-induced currents exhibit substantial variation over short spatial scales. On both widening and narrowing shelves, there is generally a marked intensification of the flow within the scattering region, and significant differences in the directions of the currents at points separated by a few tens of kilometers indicate the occurrence of rapid variations in phase. On narrowing shelves, the influence of the scattering can extend upstream into the region of uniform topography even when backscattered free waves are not possible.

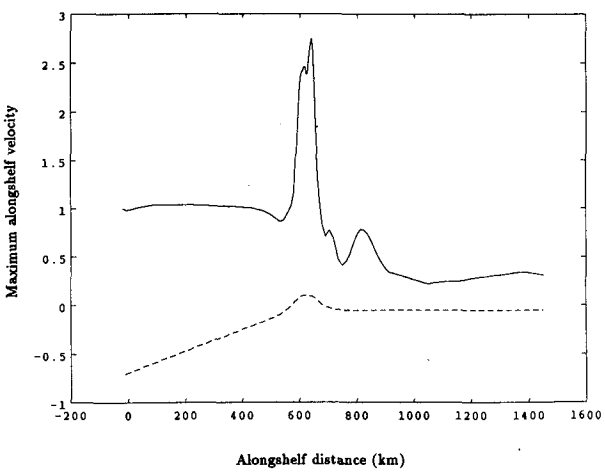

FIG. 22. Maximum surface alongshelf velocity at the coast for the FI scattering simulation. The dashed line schematically shows the location of the coast; south at the left, north at the right, and the promontory of FI in the center.

The warp factor introduced here, while somewhat ad hoc, proved useful for summarizing the narrowing shelf scattering results. This suggests that an extension of the works of Hsueh (1980) and Davis (1983) to examine further the scattering induced by nonshelf-similar topographic variations is likely to be a fruitful direction for future analytical studies. Further encouragement that the application of analytic methods to CTW scattering problems has not yet been exhausted, is the result that topographic variation and stratification apparently act independently in their contributions to CTW scattering strength. This suggests it may be possible to consider the two processes separately in an analytical study. The mixed success of the warp factor analysis when applied to the widening shelf topographies indicates that further studies, both analytical and numerical, are required to understand more fully the transfer of energy from incident to transmitted modes. In particular, we have been unable to answer the question of what physical processes determine the slope of the scattering coefficient as a function of warp factor (Figs. 6 and 8).

We have described the small spatial scale of variations in the pattern of the scattered-wave-induced currents upstream from a scattering region as the signature of evanescent wave-like motions. However, this should be considered somewhat speculative because the dynamical processes which give rise to these patterns, and the topographic features which determine the spatial scales of the evanescent waves are still unclear. A likely important consequence of the generation of intense current fluctuations extending over small spatial scales may be the increased dissipation of CTW energy through bottom friction.

A simulation was performed of CTW scattering at a site on the East Coast of Australia where observations made by Griffin and Middleton (1986) suggest the presence of scattered freely-propagating CTWs. The simulation supports Griffin and Middleton's (1986) conjecture that the waves they observed were the sig-

nature of remotely-forced free CTWs scattered by the abrupt topographic variations of their study region. This supports the notion that realistic shelf geometries can scatter significant levels of CTW energy, and that the scattered waves can have an appreciable signal in current-meter observations made on the continental shelf. Griffin and Middleton's (1986) observation of what is actually a very high mode (mode 6) free wave with a low phase speed (0.4 m s^{-1}) demonstrates that along irregular coastlines it may be necessary to account for CTW scattering processes if oceanographic observations are to be interpreted correctly. The success of the model simulation in reproducing features of Griffin and Middleton's (1986) observations suggests that simulations of free CTW scattering may be useful for predicting features of scattering processes on other continental shelves of interest, and may prove to be a useful tool for improving the design of field experiments, and the interpretation of their results.

Acknowledgments. This work was supported by the National Science Foundation under grant OCE85-21837, and by the Education Program of the Woods Hole Oceanographic Institution. Computer facilities at the National Center for Atmospheric Research in Boulder, Colorado, were used for the numerical experiments. NCAR is funded by the National Science Foundation.

REFERENCES

Allen, J. S., 1976: Continental shelf waves and alongshore variations in bottom topography and coastline. *J. Phys. Oceanogr.*, **6**, 864–878.

Battisti, D. S., and B. M. Hickey, 1984: Application of remote wind-forced coastal trapped wave theory to the Oregon and Washington coasts. *J. Phys. Oceanogr.*, **14**, 887–903.

Brink, K. H., 1980: Propagation of barotropic continental shelf waves over irregular bottom topography. *J. Phys. Oceanogr.*, **10**, 765–778.

——, 1986: Scattering of long coastal-trapped waves due to bottom irregularities. *Dyn. Atmos. Oceans*, **10**, 149–164.

——, and J. S. Allen, 1978: On the effect of bottom friction on barotropic motion over the continental shelf. *J. Phys. Oceanogr.*, **8**, 919–922.

——, and ——, 1983: Reply (to T. J. Simons' comments on K. H. Brink and J. S. Allen, *J. Phys. Oceanogr.*, **8**, 919–922). *J. Phys. Oceanogr.*, **13**, 149–150.

Buchwald, V. T., 1968: The diffraction of Kelvin waves at a corner. *J. Fluid Mech.*, **31**, 193–205.

——, 1977: Diffraction of shelf waves by an irregular coastline. *Waves on Water of Variable Depth*, D. G. Provis and R. Radok, Eds., Lecture Notes in Physics, Vol. 64, Springer and Australian Academy of Sciences, 235 pp.

Chao, S.-Y., L. J. Pietrafesa and G. S. Janowitz, 1979: The scattering of continental shelf waves by an isolated topographic irregularity. *J. Phys. Oceanogr.*, **9**, 687–695.

Chapman, D. C., 1983: On the influence of stratification and continental shelf and slope topography on the dispersion of subinertial coastally trapped waves. *J. Phys. Oceanogr.*, **13**, 1641–1652.

——, 1987: Application of wind-forced, long, coastal-trapped wave theory along the California coast. *J. Geophys. Res.*, **92**, 1798–1816.

Church, J. A., H. J. Freeland and R. L. Smith, 1986a: Coastal-trapped waves on the East Australian continental shelf, Part I: Propagation of modes. *J. Phys. Oceanogr.*, **16**, 1929–1943.

——, N. J. White, A. J. Clarke, H. J. Freeland and R. L. Smith, 1986b: Coastal-trapped waves on the East Australian continental shelf, Part II: Model verification. *J. Phys. Oceanogr.*, **16**, 1945–1957.

Clarke, A. J., and S. Van Gorder, 1986: A method for estimating wind driven frictional, time-dependent, stratified shelf and slope water flow. *J. Phys. Oceanogr.*, **16**, 1013–1028.

Cox, M. D., 1985: An eddy-resolving numerical model of the ventilated thermocline. *J. Phys. Oceanogr.*, **15**, 1312–1324.

Davis, A. M. J., 1983: Shelf similar topographies for free continental shelf waves. *Geophys. Astrophys. Fluid Dyn.* **23**, 321–331.

Freeland, H. J., F. M. Boland, J. A. Church, A. J. Clarke, A. M. G. Forbes, A. Huyer, R. L. Smith, R. O. R. Y. Thompson and N. J. White, 1986: The Australian Coastal Experiment: A search for coastal-trapped waves. *J. Phys. Oceanogr.*, **16**, 1230–1249.

Griffin, D. A., and J. H. Middleton, 1986: Coastal trapped waves behind a large continental shelf island, southern Great Barrier Reef. *J. Phys. Oceanogr.*, **16**, 1651–1664.

Haidvogel, D. B., J. L. Wilkin and R. E. Young, 1990: A semi-spectral primitive equation ocean circulation model using vertical sigma and horizontal orthogonal curvilinear coordinates. *J. Comput. Phys.*, in press.

Halliwell, G. R., and J. S. Allen, 1987: Wavenumber-frequency domain properties of coastal sea level response to alongshelf wind stress along the West Coast of North America, 1980–1984. *J. Geophys. Res.*, **92**, 11 761–11 788.

Hsueh, Y., 1980: Scattering of continental shelf waves by longshore variations in bottom topography. *J. Geophys. Res.*, **85**, 1147–1150.

Huthnance, J. M., 1978: On coastal trapped waves: Analysis and numerical calculation by inverse iteration. *J. Phys. Oceanogr.*, **8**, 74–92.

——, L. A. Mysak and D.-P. Wang, 1986: Coastal trapped waves. *Baroclinic Processes on Continental Shelves*, C. N. K. Mooers, Ed., Amer. Geophys. Union, 1–18.

Ives, D. C., and R. M. Zacharias, 1987: Conformal mapping and orthogonal grid generation, Paper No. 87-2057, AIAA/SAE/ASME/ASEE 23rd Joint Propulsion Conference, San Diego.

Killworth, P. D., 1978: Coastal upwelling and Kelvin waves with small longshore topography. *J. Phys. Oceanogr.*, **8**, 188–205.

Middleton, J. F., and D. G. Wright, 1988: Shelf wave scattering due to a longshore jump in topography. *J. Phys. Oceanogr.*, **18**, 230–242.

Mitchum, G. T., and A. J. Clarke, 1986: Evaluation of frictional, wind forced long wave theory on the West Florida shelf. *J. Phys. Oceanogr.*, **16**, 1029–1037.

Mysak, L. A., and C. L. Tang, 1974: Kelvin wave propagation along an irregular coastline. *J. Fluid Mech.*, **64**, 241–261.

Orlanski, I., 1976: A simple boundary condition for unbounded hyperbolic flows. *J. Comput. Phys.*, **21**, 251–269.

Packham, B., and W. Williams, 1968: Diffraction of Kelvin waves at a sharp bend. *J. Fluid Mech.*, **34**, 517–529.

Smith, R. L., 1978: Poleward propagating perturbations in currents and sea levels along the Peru coast. *J. Geophys. Res.*, **83**, 6083–6092.

Wang, D.-P., 1980: Diffraction of continental shelf waves by irregular alongshore geometry. *J. Phys. Oceanogr.*, **10**, 1187–1199.

Webster, I., 1987: Scattering of coastally trapped waves by changes in continental shelf width. *J. Phys. Oceanogr.*, **17**, 928–937.

Wilkin, J. L., 1987: A computer program for calculating frequencies and modal structures of free coastal-trapped waves, Tech. Rep. WHOI 87-53, Woods Hole Oceanographic Institution. 50 pp.

——, 1988a: Scattering of coastal-trapped waves by irregularities in coastline and topography, Ph.D. Thesis, Massachusetts Institute of Technology/Woods Hole Oceanographic Institution Joint Program in Oceanographic Engineering WHOI-88-47.

——, 1988b: A computer program for generating two-dimensional orthogonal curvilinear coordinate grids, *Unpublished manuscript.*

——, and D. C. Chapman, 1987: Scattering of continental shelf waves at a discontinuity in shelf width. *J. Phys. Oceanogr.*, **17**, 713–724.